The Kinetochore Protein KNL-1 Regulates Actin Cytoskeleton Dynamics to Promote Dendrite Branching in Sensory Neurons

Mattie Green[1], Henrique Alves Domingos [1], Vasilis Ouzounidis[1], Cameron Finlayson[1], Bram Prevo[1] & Dhanya K. Cheerambathur [1*]

[1]Wellcome Centre for Cell Biology & Institute of Cell Biology, School of Biological Sciences, The University of Edinburgh, Edinburgh, EH9 3BF, UK

@: Corresponding author

Email: dhanya.cheerambathur@ed.ac.uk

ABSTRACT

Precise control of dendrite branching is essential for the formation of neural circuits, yet the mechanisms that regulate this process remain poorly understood. Here we show that the kinetochore protein KNL-1, known for its role in chromosome-microtubule coupling during mitosis, together with its binding partners, the KMN network, regulate dendritic branching in the *C. elegans* mechanosensory neuron, PVD, in a cell division independent manner. Neuron-specific degradation of KNL-1 results in excess dendrite branching and fusion events, predisposes PVD to age-dependent degeneration, and impairs animal sensory behavior. Surprisingly, these effects are not attributable to mis-regulation of the microtubule cytoskeleton. Instead, KNL-1 degradation alters the dynamics of F-actin, an established driver of dendrite branching. Epistasis analysis shows that KNL-1 counters the activity of the RacGEF TIAM-1, a downstream effector of dendrite guidance receptors. These findings establish that the microtubule coupling KMN network promotes dendrite branching by regulating the actin cytoskeleton and provide insight into how the cytoskeleton shapes dendritic architecture.

KEY WORDS: cytoskeleton, actin, microtubule, kinetochore, dendrite, neurodevelopment, dendrite morphogenesis, dendrite arborization, KNL-1, TIAM-1, PVD neuron

INTRODUCTION

Neurons have specialized compartments for transmitting information, including dendrites, which receive & integrate signals, and axons, which propagate them. The shape, size and trajectory of dendritic and axonal processes determines how a neuron communicates and functions. Dendrites display diverse shapes and complex branching patterns that are unique to neuronal types[1]. The dendrite arborization pattern defines how input signals are distributed and integrated, ultimately shaping the functional properties of neurons and their connectivity within the neural circuits. Proper development and organization of dendritic arbors is therefore crucial for establishing the neural circuits, which regulate animal behavior. Notably, alterations in dendrite morphology and organization are associated with several neurodevelopmental & neurodegenerative disorders [2].

Dendrite morphogenesis initiates when extrinsic guidance cues interact with specific cell surface receptors on the neuron and activate intracellular signaling pathways that trigger cytoskeletal rearrangements to enable dendrite growth and branching [2]. The Rho family of GTPases (Cdc-42, Rac1, and RhoA) are key downstream effectors of the guidance cues during dendrite development[3–6]. Rho GTPases influence dendrite arborization by regulating actin filament assembly and the formation of actin structures such as filopodia and lamellipodia. During dendrite outgrowth, dynamic actin filaments form a network of lamellipodial and filopodial protrusions that guide and propel the growth cone. Dendritic arborization occurs when filopodia emerge from preexisting branches and undergo extension and retraction until they become stabilized[7]. Consequently, dendrite arbor growth and stabilization entail extensive actin remodeling and careful coordination between actin growth states and structures. Various actin regulators, including F-actin nucleators modulators of F-actin dynamics, have been shown to affect dendrite morphogenesis [8,9] . However, it is unclear

38 how the activity of different actin regulators is coordinated and controlled spatially &
39 temporally by the Rho GTPases to generate a specific dendrite pattern.

40 The microtubule cytoskeleton is also critical for dendrite morphogenesis. Microtubules
41 provide structural support for dendrites and serve as tracks to transport key building materials
42 and organelles. Mutations in molecular motors that affect transport severely impair dendrite
43 morphology, and loss of microtubules-associated proteins result in dendrite development
44 defects[10–14]. In addition, microtubule nucleators are found at branch points of developing
45 dendrites, where they organize microtubule arrays to regulate branching[15]. Studies on the
46 role of microtubules in dendritic spines, small actin-rich protrusions on dendrite branches that
47 are sites of high synaptic activity, have shown that dynamic microtubules enter the actin-rich
48 spines in a synaptic-activity-dependent manner and that this is facilitated by actin
49 cytoskeleton remodeling[12,16,17]. Thus, a crosstalk between the two cytoskeletal structures
50 appears to exist within dendrites, but its molecular basis remains elusive.

51 Recent studies have revealed that kinetochore proteins, which connect chromosomes
52 to dynamic spindle microtubules in dividing cells, also play an unexpected post-mitotic role
53 during neurodevelopment. The conserved 10-subunit Knl1 complex/Mis12 complex/Ndc80
54 complex (KMN) network, which serves as the primary chromosome-microtubule coupler[18,19],
55 is enriched along developing dendrites of *C. elegans* sensory neurons and in the synapses
56 and axons of *D. melanogaster* neurons [20,21]. Depletion of any KMN component in *C. elegans*
57 sensory neurons results in dendrite growth defects, indicating that KMN function is critical for
58 dendrite development. Knockdown of Mis12 causes dendrite branching defects in *D.*
59 *melanogaster* embryonic sensory neurons and increases filopodial protrusions in dendrites
60 of rat hippocampal neurons, underscoring the importance of the Mis12 complex for proper
61 dendrite formation. Moreover, kinetochore proteins promote dendrite regeneration of *D.*

62 *melanogaster* sensory neurons, highlighting their involvement in the maintenance of dendrite
63 morphology [22].

64 The mechanisms by which kinetochore proteins contribute to dendrite development
65 and maintenance is not understood, but some observations imply that microtubule binding
66 activity is important [20,22]. The neuronal function of KMN network in *C. elegans* sensory
67 neurons depends on the microtubule coupling interface within the Ndc80 complex.
68 Additionally, knockdown of kinetochore proteins in *D. melanogaster* sensory neurons
69 increases the number of microtubule plus ends in dendrites, suggesting a role in the
70 regulation of microtubule dynamics[22].

71 Our previous characterization of the KMN network's post mitotic role in neurons
72 focused on dendrite extensions of the *C. elegans* amphid sensory neuron bundles, which
73 consist of 12 dendrites from 12 neurons[20]. This precluded a detailed analysis of cellular
74 structures within dendrites at the single-neuron level. To overcome this limitation, we have
75 examined the role of KNL-1 during dendrite branching of the mechanosensory neuron PVD.
76 Dendrite development in PVD is stereotypical and invariant, and its cytoskeletal organization
77 is well characterized, making it a good system to investigate kinetochore protein function. In
78 this study we demonstrate that KNL-1 is concentrated in the extending dendrites processes
79 and at branch points, and that PVD-specific degradation of KNL-1 perturbs higher order
80 branch formation, leading to behavioral defects and premature neurodegeneration.
81 Surprisingly, KNL-1 degradation does not affect microtubule organization or dynamics, but
82 instead up-regulates F-actin assembly in the cell body and primary dendrites. We show that
83 KNL-1 acts antagonistically to the RacGEF TIAM-1, the downstream effector of dendrite
84 branching cues. Thus, the kinetochore protein KNL-1 contributes to the dendrite guidance
85 pathway through regulation of the neuronal actin cytoskeleton.

RESULTS

86 **KNL-1 localizes to developing dendrites in the PVD neuron**

87 The PVD neuron in *C. elegans* is a type of mechanosensory neuron located between the
88 body wall muscle and the epidermis of the animal. A unique feature of the PVD is the highly
89 arborized dendrites that extend throughout the animal's body. **(Figure 1A)**. PVD dendrites
90 form a distinctive branching pattern composed of non-overlapping repeating units called
91 "menorahs", which are important for integrating and processing sensory inputs **(Figure 1A)**[23].
92 PVD dendrite branches are established during the larval stages and the branching follows a
93 stereotypical developmental program that begins at the late L2 larval stage and concludes by
94 the late L4 larval stage **(Figure S1A)**. To visualize the localization of the kinetochore protein
95 KNL-1 in the PVD neuron, we used a split-GFP system[24]. The N-terminus of KNL-1 was fused
96 to 7 copies of the β11 strand of GFP at the endogenous locus, and the complementing GFP
97 1-10 was expressed under a PVD-specific promoter. The cell body of PVD is located near
98 the animal tail, and two primary (1°) dendrites extend from the cell body towards the anterior
99 and posterior. KNL-1 was enriched in the cell body and along the extending 1° dendrites at
100 the L2 larval stage **(Figure 1B)**. During the L3 and L4 stages, higher order branches develop
101 from the 1° dendrite to generate the distinctive menorah shape. KNL-1 signal persisted along
102 the 1° dendrites in the L3 and L4 stages but became more punctate **(Figure S1B)**. We also
103 observed discrete KNL-1 puncta at the base of branch points of 2° dendrite and 3° dendrites,
104 as well as along the newly formed 3° dendrites **(Figures 1C, 2D & S1B-D)**. These results
105 indicated that KNL-1 may play a role in PVD dendrite formation.

KNL-1 functions cooperatively with the KMN network to restrict dendritic branching

106 To investigate the function of KNL-1 in the PVD neuron, we utilized an auxin inducible degron
107 (AID) to selectively degrade KNL-1 in the PVD neuron (KNL-1 degrader). We fused an AID
108 peptide sequence along with GFP to KNL-1 at the endogenous locus and expressed the plant
109 specific F-box protein TIR1 under PVD-specific promoters **(Figure 2A)**[25,26]. To degrade KNL-
110 1, we synchronized the worms as L1 larvae and exposed them to auxin at the L2 stage when
111 PVD development is initiated **(Figure S2A)**. We observed a significant reduction in
112 GFP::KNL-1 signal from the PVD cell body at the L2 stage **(Figure 2A)**. To assess the effect
113 of KNL-1 degradation on PVD development, we visualized dendrite morphology in L4 larvae
114 by expressing a plasma membrane (pleckstrin homology domain, PH) marker. Both control
115 and KNL-1 degrader neurons exhibited proper extension of their 1° dendrites**.** However, we
116 observed a significant disruption of the higher-order branching pattern following KNL-1
117 degradation **(Figures 2B & S2F)**. Menorahs consist of dendrite branches that are arranged
118 at right angles with respect to each other. Specifically, each menorah contains a 2° dendrite
119 that branches off at a right angle from the 1° dendrite, which then gives rise to an orthogonal
120 3° branch that forms the base of menorah. Finally, several smaller 4° dendrites emerge at
121 right angles to the 3° dendrite to complete the menorah. The number of 2° dendrite branches
122 was not significantly different between control and KNL-1 degrader neurons **(Figure S2B).**
123 However, KNL-1 degrader neurons exhibited an increased number of 4° dendrite branches
124 **(Figure 2C)**, an increased number of fusion events between 3° dendrites **(Figure 2D)**, and
125 an increased number of ectopic neurites originating from the 1° dendrites **(Figure S2C)**.

126 We next overexpressed KNL-1 in the PVD neuron by generating extrachromosomal
127 arrays that contain multiple copies of transgenic KNL-1::GFP under a PVD-specific promoter.
128 Compared to control animals that contained a GFP-expressing plasmid in the array, animals

129 with KNL-1::GFP arrays exhibited a decrease in higher-order branching. Specifically, the
130 number of 2° and 4° dendrite branches were significantly reduced **(Figures 2H, 2I & S2J)**.
131 We conclude that PVD-specific degradation and overexpression of KNL-1 have opposite
132 effects on higher-order dendritic branching.

133 We also investigated the effect of degrading the Mis12 and the Ndc80 complexes
134 within the KMN network on PVD branching. Degradation of KNL-3 (a component of the Mis12
135 complex) or Ndc80 disrupted PVD dendrite architecture in a similar manner to KNL-1
136 degradation **(Figure S2E-I)**. Taken together, these results reveal that PVD-localized KNL-1
137 functions in the context of the KMN network to restrict dendritic branching. We conclude that
138 the kinetochore-microtubule coupling machinery has a crucial role in ensuring proper PVD
139 dendrite arborization.

KNL-1 regulates the dynamics and stability of dendrite branches

140 A prominent effect of KNL-1 degradation is the fusion of neighboring menorahs resulting from
141 the merging or overlap of 3° dendrites **(Figure 2D)**. In control neurons, 3° dendrites of
142 neighboring menorahs do not overlap with each other because they quickly retract after
143 contacting each other. The aberrant fusion observed following KNL-1 degradation and the
144 presence of GFP::KNL-1 puncta along the 3° dendrite and at branch points within the
145 menorah **(Figures 1C & S2I)** suggests that KNL-1 plays a role in resolving contacts between
146 the growing tips of neighboring 3° dendrites. To understand how KNL-1 contributes to the
147 spatial separation of menorahs, we tracked the growth dynamics of 3° dendrites. Consistent
148 with previous studies [23,27], 3° dendrites of neighboring menorahs retracted within 5-10 min of
149 mutual contact in control neurons **(Figure 2E, 2G)**. In KNL-1 degrader neurons, the frequency
150 with which neighboring 3° dendrites established contact remained unchanged **(Figure S2D)**

151 but contact duration was longer **(Figure 2G)**. The presence of persistent contacts after KNL-
152 1 degradation resulted in a higher frequency of unresolved fusions, indicating that KNL-1
153 function ensures timely retraction of 3° dendrites during menorah formation **(Figure 2F)**.
154 These observations suggest that KNL-1 regulates the dynamics and stability of dendrite
155 branches to establish the highly ordered branching pattern of PVD neurons.

KNL-1 degradation impairs function and lifespan of the PVD neuron

156 As KNL-1 function is essential for proper dendrite arborization in the PVD neuron, we next
157 examined the sensory behavior of KNL-1 degrader animals. Proprioception, awareness of
158 body position and movement, is attributed to PVD dendrites that sense mechanical stimuli
159 and provide feedback to the body wall muscles to generate a stereotypical sinusoidal
160 locomotory pattern **(Figure 3A)**. To determine the body posture of animals, we visualized
161 their movement on food and measured wavelength and amplitude of their sinusoidal tracks.
162 As a positive control, we used animals lacking DMA-1, a transmembrane receptor that is
163 essential for PVD dendrite formation. KNL-1 degrader animals showed reduced amplitudes
164 and wavelengths, indicating that degradation of KNL-1 in the PVD neuron impairs
165 proprioception **(Figures 3A - C)**.

166 Analysis of PVD morphology at the L4 stage revealed that dendrites of KNL-1
167 degrader neurons contained more bead-like structures compared to control neurons **(Figures**
168 **3D, 3E)**. Beading is implicated in age-dependent decline of PVD dendrites [28], and substantial
169 beading does not appear until late into adulthood (Day 6) in control neurons. The presence
170 of substantial beading at the L4 stage suggested that KNL-1 degrader neurons degenerate
171 prematurely. Age-dependent degeneration of PVD dendrites is mediated by the autophagy
172 pathway [28], and autophagosomes marked by mScarlet-I::LGG-1 were enriched in dendrites

173 of KNL-1 degrader neurons at the day 1 adult stage **(Figure 3F, 3G)**. These observations
174 suggest that KNL-1 degradation predisposes the PVD neuron to premature ageing.

KNL-1 degradation does not perturb PVD polarity, microtubule organization, or microtubule dynamics

175 The canonical role of KMN network proteins is to stabilize the interactions between
176 chromosomes and microtubules during chromosome segregation. Microtubule function and
177 stability are also critical for the establishment and maintenance of neuronal polarity in the
178 PVD neuron [11,29,30]. Therefore, we hypothesized that KNL-1 could affect PVD dendrite
179 branching by regulating the underlying microtubule architecture and neuronal polarity. To
180 determine whether KNL-1 degradation impacts PVD polarity, we assessed the distribution of
181 RAB-3, a small GTPase associated with synaptic vesicles, and DMA-1, which localizes
182 exclusively to dendrites **(Figure 4A)**. We observed no change in the distribution of either
183 RAB-3 or DMA-1 following KNL-1 degradation, indicating that PVD polarity remains intact
184 **(Figure 4B 4C & S3A, S3B)**.

185 Next, we investigated whether KNL-1 degradation impacts the distribution, dynamics,
186 or stability of microtubules in the 1° anterior dendrite. To monitor microtubule orientation and
187 dynamics we imaged the microtubule plus end-tracking protein $EB1^{EBP-2}$, which binds to
188 growing microtubule plus ends. $EB1^{EBP-2}$::GFP was expressed under a PVD-specific
189 promoter, and its trajectories were followed by time-lapse imaging in L4 larvae **(Figure 4D)**.
190 In control neurons, the majority of the $EB1^{EBP-2}$::GFP puncta moved towards the cell body,
191 which is consistent with previous observations [10,31] that within the 1° anterior dendrite
192 microtubules are oriented with their minus end distal **(Figure 4D & 4E)**. There was no
193 significant difference in the direction of movement, velocity, or frequency of $EB1^{EBP-2}$::GFP

194 comets in KNL-1 degrader neurons **(Figure 4D, 4E & S3D, S3E)**. Thus, KNL-1 does not
195 contribute to the orientation, distribution, or dynamics of microtubule plus ends within PVD
196 dendrites.

197 We also examined tubulin distribution and microtubule stability in PVD dendrites by
198 expressing an α-tubulin GFP-fusion protein. GFP::TBA-1 is enriched in 1° dendrites and is
199 not detectable in higher-order dendrite branches of control animals, and this distribution was
200 not affected by KNL-1 degradation **(Figure S3C)**. To assess the stability of microtubules, we
201 performed Fluorescence Recovery After Photobleaching (FRAP) experiments on
202 microtubules labeled with endogenous GFP::TBA-1 using the split-gfp system **(Figure 4F)**.
203 After KNL-1 degradation, microtubules within the 1° anterior dendrite recovered to a similar
204 extent (~20%) and with the same kinetics as microtubules in control neurons **(Figure 4F &**
205 **S3F)**. Recovery kinetics indicate that microtubules in the 1° anterior dendrite are largely
206 stable, and that microtubule stability is not impaired by KNL-1 degradation. Overall, these
207 experiments indicate that altered neuronal polarity or perturbed microtubule organization and
208 dynamics are unlikely to account for the striking effect of KNL-1 loss on PVD dendritic
209 branching and consequent impairment of PVD neuron function and lifespan.

KNL-1 limits F-actin assembly and dynamics in the PVD cell body and dendrites

210 During our analysis of PVD morphology, we noticed that the cell body in KNL-1 degrader
211 animals was enlarged and deformed **(Figure 5A, 5B)**, suggestive of defects associated with
212 the actin cytoskeleton. To visualize the actin cytoskeleton during PVD dendrite branching, we
213 generated a strain expressing Lifeact, the actin binding peptide of the yeast protein Abp140,
214 fused to mKate2 under a PVD-specific promoter. We imaged actin and the plasma membrane
215 of the PVD neuron at the L4 stage, when 4° dendritic branches are beginning to form. In

216 control neurons, Lifeact::mKate2 signal is enriched in the 3° and 4° dendrites compared to
217 the 1° dendrites and the cell body, consistent with previous observations [32,33] that newly
218 formed dendrites show a higher concentration of F-actin **(Figure 5C)**. In KNL-1 degrader
219 neurons, Lifeact::mKate2 signal intensity in the cell body and proximal 1° dendrites was
220 significantly increased **(Figure 5C),** and close examination revealed prominent F-actin cables
221 in the cell body of KNL-1 degrader neurons **(Figure 5D-G & S4A-C)**. These results suggest
222 that degradation of KNL-1 during PVD development results in increased F-actin levels.

223 To assess F-actin dynamics, we performed FRAP in the 1° anterior dendrite. In both
224 control and KNL-1 degrader neurons, recovery of Lifeact::mKate2 signal was slow suggesting
225 a low turnover rate for F-actin. However, the extent of recovery was significantly lower in KNL-
226 1 degrader neurons (8% vs. 14% in controls) indicative of a higher fraction of stable F-actin
227 structures **(Figure 5H, 5I)**.

228 Consistent with a role for KNL-1 in regulating F-actin dynamics, we found that KNL-1
229 influences the dynamics of filopodial protrusions from 1° dendrites. 2° dendrite branches
230 initiate when several actin-rich filopodial like projections extend orthogonally from the 1°
231 dendrite. Most of these filopodia undergo several cycles of extension and retraction until a
232 subset of projections stabilize to form the 2° dendrites **(Figure S4D)**. The number of filopodial
233 protrusions from 1° dendrites was significantly increased in KNL-1 degrader neurons **(Figure**
234 **5J, 5K & S4D)**. Unlike the filopodial outgrowths in control dendrites, which extend
235 orthogonally for a short period, protrusions in KNL-1 degrader dendrites had a longer lifetime
236 and arbitrary trajectories, often running parallel to 1° dendrites **(Figure 4SD)**. These
237 observations suggest that KNL-1 plays a critical role in regulating filopodial generation and
238 dynamics in 1° dendrites.

KNL-1 acts antagonistically to the RacGEF TIAM-1 to promote dendrite branching

239 Since KNL-1 regulates F-actin and dendrite branch dynamics as well as menorah formation,
240 we investigated how it connects with the molecular pathway that controls F-actin remodeling
241 and dendrite branching. Dendrite branching is driven by actin polymerization, which is
242 triggered by Rho family GTPases activated in response to guidance cues [9]. Specifically, the
243 adhesion molecules L1CAM/SAX-7 and MNR-1 in the epidermis interact with DMA-1/LRR,
244 the dendrite guidance receptor on the surface of the PVD neuron to initiate the formation of
245 3° and 4° branches . Within the PVD neuron, DMA-1 in conjunction with HPO-30, the claudin-
246 like transmembrane protein, functions as a scaffold for the RacGEF TIAM-1 and the Arp2/3
247 complex activator WRC (Wave Regulatory Complex) to promote actin assembly and drive
248 dendrite branching **(Figure 6A)**. To determine whether KNL-1 acts in the DMA-1-mediated
249 F-actin assembly pathway, we performed epistasis analysis of PVD-specific KNL-1
250 degradation with mutants in the *dma-1*-mediated branching pathway. Deletion of *dma-1*
251 results in complete loss of branching and menorah formation. Combining KNL-1 degradation
252 with a *dma-1Δ* mutant resulted in a similar phenotype as *dma-1Δ* alone, suggesting that KNL-
253 1 functions downstream of DMA-1.

254 We next tested the genetic interaction between KNL-1 and TIAM-1. TIAM-1 is
255 essential for higher order branching, as *tiam-1Δ* PVD neurons exhibit "immature" menorahs
256 that lack 4° branches **(Figure 6B, 6C)**. KNL-1 degradation in the PVD suppressed the
257 branching defects observed in *tiam-1Δ* animals and led to complete restoration of the
258 menorahs and the 3° and 4° branch counts **(Figure 6B-D)**. This suggests that KNL-1
259 degradation compensates for the loss of *tiam-1* by promoting dendrite branching. Additionally,
260 the menorah fusion defects observed in KNL-1 degrader neurons were reduced in *tiam-1Δ*

261 animals, indicating that KNL-1 and TIAM-1 have opposing effects on menorah formation
262 **(Figure 6E)**.

263 TIAM-1 is a RacGEF proposed to locally recruit active Rac to initiate F-actin assembly.
264 Interestingly, in addition to the suppression of branching defects, *tiam-1Δ* also suppressed
265 the cell body shape defects of KNL-1 degrader neurons **(Figure 6F, 6G)**. Consistent with this
266 rescue, we found that F-actin levels in the cell body were no longer increased when KNL-1
267 was degraded in the *tiam-1Δ* background **(Figure 6G-I)**. Given that *tiam-1Δ* rescued F-actin
268 levels in KNL-1 degrader neurons, we were surprised to find that *tiam-1Δ* on its own increased
269 F-actin levels to a similar extent as KNL-1 degradation **(Figure 6G-I)**. This indicates that
270 TIAM-1 does not solely function as a GEF that promotes actin polymerization, and further
271 work will be necessary to understand the role of TIAM-1 in F-actin regulation and its epistatic
272 effect with KNL-1 degradation. Overall, these results demonstrate that KNL-1 and TIAM-1 act
273 antagonistically to modulate actin polymerization dynamics to promote the branching and
274 proper patterning of dendrite architecture of the PVD neuron.

DISCUSSION

275 Dendrite morphogenesis is a highly orchestrated process that requires precise regulation of
276 the actin and microtubule cytoskeleton. Various effectors of cytoskeletal remodeling in
277 dendrites have been identified, but how effector functions are coordinated to generate the
278 unique dendrite pattern of each neuron remains largely undefined. Taking advantage of the
279 unique morphology of the PVD neuron and a PVD-specific protein-degradation system, we
280 show that the kinetochore component KNL-1 facilitates dendrite arborization, and that it does
281 so in the context of the KMN network, the microtubule-coupling machine that drives
282 chromosome segregation during cell division.

283 KNL-1 degradation does not appreciably affect microtubule organization or growth
284 dynamics in PVD dendrites, nor does it affect PVD polarity, which is consistent with
285 observations in *D. melanogaster* sensory neurons[22]. KNL-1 degradation also has no effect
286 on the abundance of EB1-marked microtubule plus ends, which contrasts with the increased
287 number of EB1 comets observed after knockdown of Ndc80 and Mis12 subunits in *D.*
288 *melanogaster* neurons. KNL-1 function therefore appears to differ significantly from that of
289 other known microtubule-associated proteins in PVD, whose inhibition primarily affects
290 neuronal polarity or microtubule orientation and stability [10,29,30,34].

291 Taken together, our results argue against the idea that KNL-1 facilitates dendrite
292 branching through regulation of the microtubule cytoskeleton. Instead, we unexpectedly
293 found that KNL-1 degradation increases F-actin levels in the cell body and primary dendrites
294 and promotes formation of filopodial protrusions from primary dendrites, which suggested to
295 us that KNL-1 might regulate actin filament dynamics. Furthermore, the observed increase in
296 filopodial protrusions after Mis12 knockdown in rat hippocampal neurons is consistent with
297 the idea that other components of the KMN network may also affect the actin cytoskeleton[21].
298 It remains to be determined whether KNL-1's effect on actin requires association of the KMN
299 network with microtubules. We note, however, that KNL-1 does not appear to be specifically
300 enriched at microtubule-based structures (data not shown), and that fluorescence microscopy
301 suggests microtubules are absent in 3° and 4° dendrites, where KNL-1 presumably acts
302 during dendrite branching [11,35].

303 Recent studies suggest that dendrite branching results from a balance of F-actin-
304 dependent dendrite growth and retraction, and our time lapse analysis shows that KNL-1
305 degradation primarily inhibits branch retraction [27,35]. At the molecular level, dendrite branching
306 in PVD is driven by synergistic interaction between DMA-1, the transmembrane guidance

307 receptor, and HPO-30, the claudin superfamily member[32,33]. DMA-1 & HPO-30 are thought
308 to independently recruit the WAVE regulatory complex (WRC) to promote Arp2/3 mediated
309 assembly of branched F-actin networks, with DMA-1 recruiting WRC via the RacGEF TIAM-
310 1, and HPO-30 recruiting WRC directly through its C-terminal domain. TIAM-1 is essential to
311 form 3° & 4° branching[32,33], and we show that KNL-1 degradation rescues the branching
312 defects observed in *tiam-1Δ*. Moreover, the KNL-1 degradation phenotype in PVD is similar
313 to that of TIAM-1 or DMA-1 overexpression. This suggests that KNL-1 functions in the DMA-
314 1 pathway and promotes dendrite branching by antagonizing TIAM-1-mediated F-actin
315 assembly. A parsimonious explanation would be that KNL-1 counters the GEF activity of
316 TIAM-1. However, this is contradicted by the observation that the GEF activity of TIAM-1 is
317 not essential for dendrite branching.

318 An emerging view is that a balance between linear and branched actin filaments
319 underlies the transition from extension to retraction of the growing 3° dendrites[35].
320 Interestingly, previous work showed that Formin, a nucleator of linear actin filaments, is
321 enriched at kinetochores of human cultured cells and contributes to the stability of
322 kinetochore-attached microtubules during mitosis in mammalian cells and during meiosis in
323 oocytes[36–38]. Moreover, a recent study showed that F-actin cables generated by Formin and
324 Spire, another nucleator of linear actin filaments, interact with kinetochores during porcine
325 oocyte meiosis[39]. Given this close link between kinetochores and Formin, an attractive
326 hypothesis to be tested in the future is that the PVD-localized KMN network regulates linear
327 F-actin assembly during dendrite outgrowth, thereby ensuring the balance between linear and
328 branched F-actin filaments required for proper dendrite arborization.

ACKNOWLEDGMENTS

We thank Reto Gassmann and Rebecca Green for comments on the manuscript. This work is supported by a Sir Henry Wellcome Postdoctoral Fellowship (215925) to B.P. and a Sir Henry Dale Fellowship (208833) to D.K.C. Imaging was performed in Centre Optical Instrumentation Laboratory (COIL), which is supported by a Core Grant (203149) to the Wellcome Centre for Cell Biology at the University of Edinburgh. Some strains were provided by the CGC, which is funded by NIH Office of Research Infrastructure Programs (P40 OD010440)

DECLARATION OF INTERESTS

The authors declare no competing interests.

Figure 1

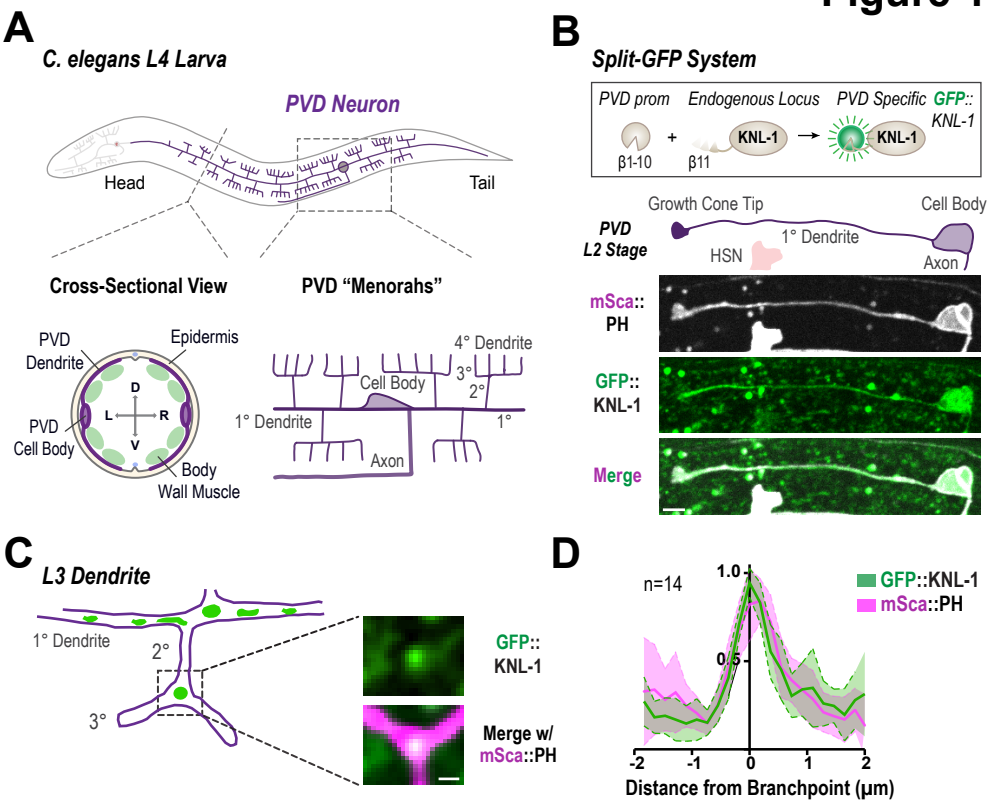
A
C. elegans L4 Larva
PVD Neuron
Head
Tail
Cross-Sectional View
PVD "Menorahs"
PVD Dendrite
Epidermis
D
L
R
V
PVD Cell Body
Body Wall Muscle
4° Dendrite
3°
2°
Cell Body
1° Dendrite
1°
Axon
B
Split-GFP System
PVD prom
Endogenous Locus
PVD Specific
GFP::KNL-1
β1-10
β11
KNL-1
KNL-1
Growth Cone Tip
Cell Body
PVD L2 Stage
1° Dendrite
HSN
Axon
mSca::PH
GFP::KNL-1
Merge

C
L3 Dendrite
1° Dendrite
2°
3°
GFP::KNL-1
Merge w/ mSca::PH
D
n=14
1.0
0.5
GFP::KNL-1
mSca::PH
-2
-1
0
1
2
Distance from Branchpoint (µm)

Figure 1. KNL-1 localisation in the PVD neuron.

337 **(A)** Schematic of the PVD neuron at the L4 larval stage. The left inset cartoon shows a cross-
338 sectional view of PVD between the epidermis and body wall muscle. The right inset illustrates
339 the discrete “menorah”-like dendrite branching pattern of the PVD neuron. **(B)** Localization of
340 GFP::KNL-1 expressed specifically in PVD neuron using a split-GFP system. The image
341 represents an L2 stage PVD neuron which has begun to extend its anterior dendrite. Scale
342 bar, 5μm. **(C)** An example, with a schematic, of GFP::KNL-1 localizing at the developing
343 branch points in an L3 stage PVD dendrite. Scale Bar, 1μm. **(D)** Quantification of GFP::KNL-
344 1 at the intersections of 2° and 3° dendrites as shown in (C).
345

Figure 2

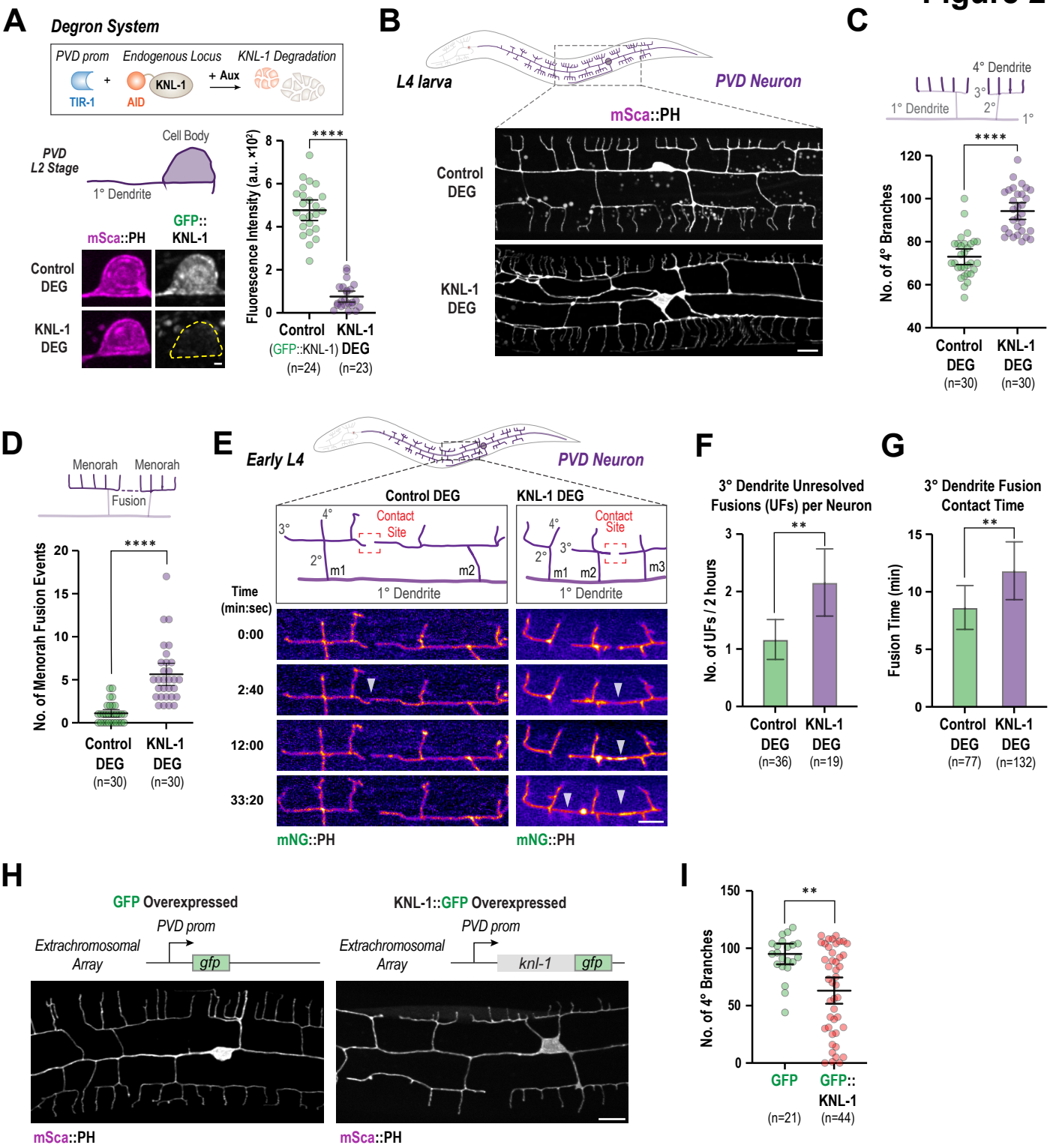
A
Degron System
PVD prom
Endogenous Locus
KNL-1 Degradation
TIR-1
AID
KNL-1
+ Aux
PVD L2 Stage
Cell Body
1° Dendrite
mSca::PH
GFP::KNL-1
Control DEG
KNL-1 DEG
Fluorescence Intensity (a.u. x10³)
****
Control (GFP::KNL-1)
KNL-1 DEG
(n=24)
(n=23)
B
L4 larva
PVD Neuron
mSca::PH
Control DEG
KNL-1 DEG
C
4° Dendrite
3°
1° Dendrite
2°
1°
No. of 4° Branches
****
Control DEG
KNL-1 DEG
(n=30)
(n=30)
D
Menorah
Menorah
Fusion
No. of Menorah Fusion Events
****
Control DEG
KNL-1 DEG
(n=30)
(n=30)
E
Early L4
PVD Neuron
Control DEG
KNL-1 DEG
Contact Site
1° Dendrite
Time (min:sec)
0:00
2:40
12:00
33:20
mNG::PH
mNG::PH
F
3° Dendrite Unresolved Fusions (UFs) per Neuron
No. of UFs / 2 hours
**
Control DEG
KNL-1 DEG
(n=36)
(n=19)
G
3° Dendrite Fusion Contact Time
Fusion Time (min)
**
Control DEG
KNL-1 DEG
(n=77)
(n=132)
H
GFP Overexpressed
PVD prom
Extrachromosomal Array
gfp
KNL-1::GFP Overexpressed
PVD prom
Extrachromosomal Array
knl-1
gfp
mSca::PH
mSca::PH
I
No. of 4° Branches
**
GFP
GFP::KNL-1
(n=21)
(n=44)

346 **Figure 2. KNL-1 is required for proper dendrite branching of the PVD neuron.**

347 **(A)** Approach used to degrade endogenously tagged AID::KNL-1 in the PVD neuron (top).
348 Images below show loss of GFP::KNL-1 signal in presence of PVD-specific Tir1 transgene &
349 auxin. The plot on the right shows the mean fluorescence intensity of the GFP signal in the
350 cell body for control & KNL-1 DEG. Scale bar, 1μm. **(B)** Images of PVD dendrite organization
351 in the control (top) & KNL-1 DEG (bottom). Scale bar, 10μm. **(C&D)** Quantification of PVD
352 dendrite organization in terms of 4° branch count and fusion between menorahs in control &
353 KNL-1 DEG. **(E)** Stills from time-lapse imaging of 3° dendrite branch dynamics in control &
354 KNL-1 DEG animals. White arrow heads denote fusion events between two adjacent
355 menorahs. Scale bar, 5μm. **(F)** Quantification of the number of fusion events between 3°
356 dendrites of two adjacent menorahs that remained unresolved during the time lapse. n
357 corresponds to the total number of animals analyzed in each condition. **(G)** Quantification of
358 time spent in contact by 3° dendrites of two adjacent menorahs. n corresponds to the total
359 events analyzed in control animals and KNL-1 DEG animals. **(H)** Images of PVD in control
360 (GFP) (left) & KNL-1 GFP overexpressing animals (right). Scale bars, 10μm. **(I)** Quantification
361 of the number of 4° branches in the PVD in control (GFP) and KNL-1::GFP overexpressing
362 animals.

363

Figure 3

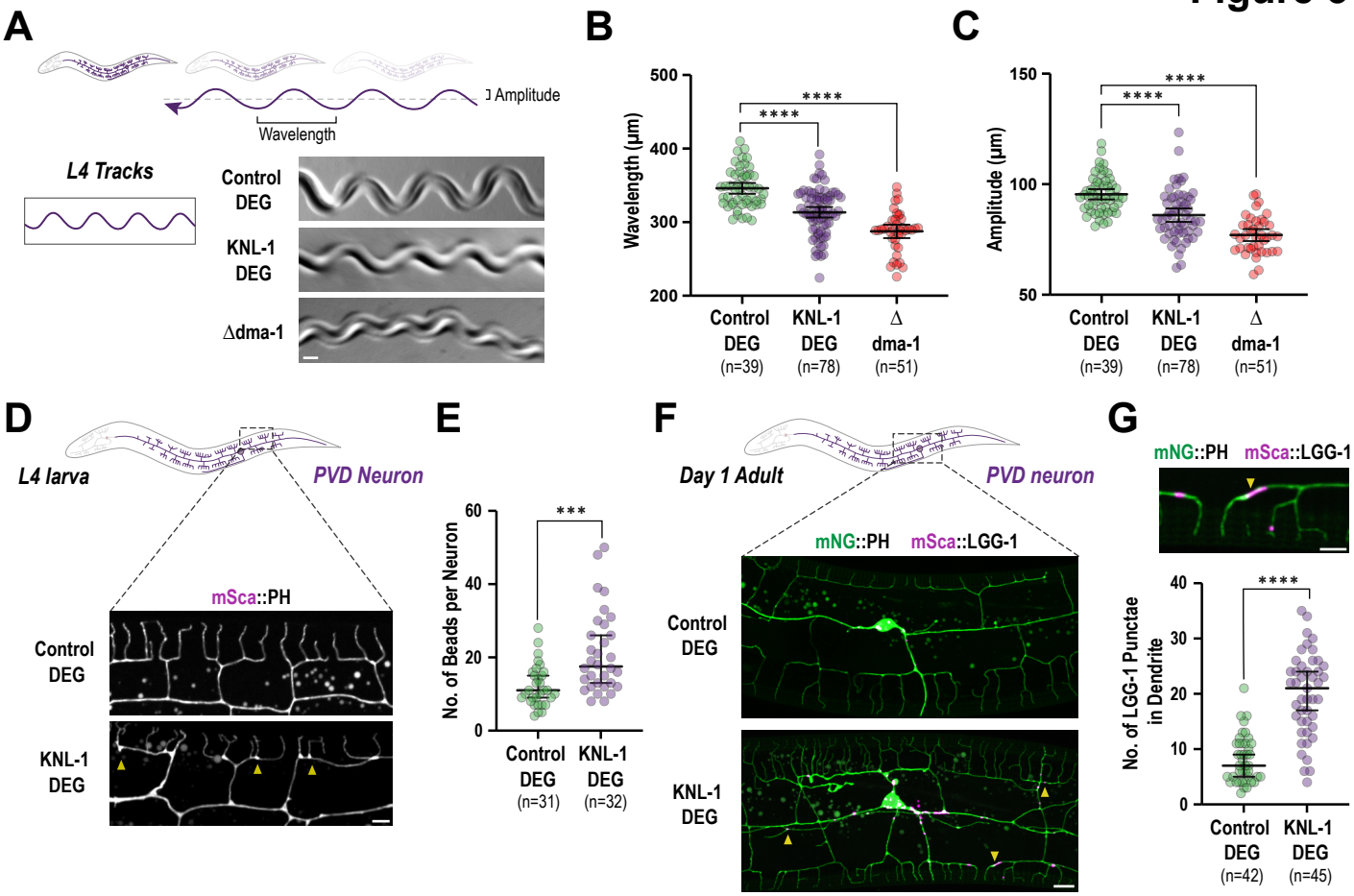
A
Amplitude
Wavelength
L4 Tracks
Control DEG
KNL-1 DEG
Δdma-1
B
Wavelength (µm)
500
400
300
200
****
****
Control DEG (n=39)
KNL-1 DEG (n=78)
Δ dma-1 (n=51)
C
Amplitude (µm)
150
100
50
****
****
Control DEG (n=39)
KNL-1 DEG (n=78)
Δ dma-1 (n=51)
D
L4 larva
PVD Neuron
mSca::PH
Control DEG
KNL-1 DEG
E
No. of Beads per Neuron
60
40
20
0
***
Control DEG (n=31)
KNL-1 DEG (n=32)
F
Day 1 Adult
PVD neuron
mNG::PH
mSca::LGG-1
Control DEG
KNL-1 DEG
G
mNG::PH
mSca::LGG-1
No. of LGG-1 Punctae in Dendrite
40
30
20
10
0
****
Control DEG (n=42)
KNL-1 DEG (n=45)

364 **Figure 3. KNL-1 is important for proprioceptive behavior and PVD neuron maintenance.**
365 **(A)** Proprioception behavior analysis**.** Representative tracks of animals in indicated
366 conditions**.** The wild type control worms form sinusoidal tracks. Scale bar, 20μm **(B&C)**
367 Quantification of the wavelength and amplitude of the tracks by animals in indicated
368 conditions. **(D)** Images of PVD dendrite organization in the control (top) & KNL-1 DEG
369 (bottom) animals. Yellow arrowhead indicates the bead-like blebs seen with membranes.
370 Scale bar, 5μm. **(E)** Quantification of the bead-like blebs in control and KNL-1 DEG animals.
371 **(F)** Autophagosomes labeled with the marker mScarlet-I::LGG-1 overlaid with membrane
372 (mNeonGreen::PH) in control & KNL-1 DEG adult animals. Yellow arrowheads indicate the
373 appearance of LGG-1 puncta along the dendrites. Scale bar, 10μm. **(G)** Quantification of
374 mScarlet-I::LGG-1 puncta in the dendrites in control & KNL-1 DEG animals. Yellow
375 arrowhead indicates an LGG-1 puncta. Scale bar, 5μm.
376

Figure 4

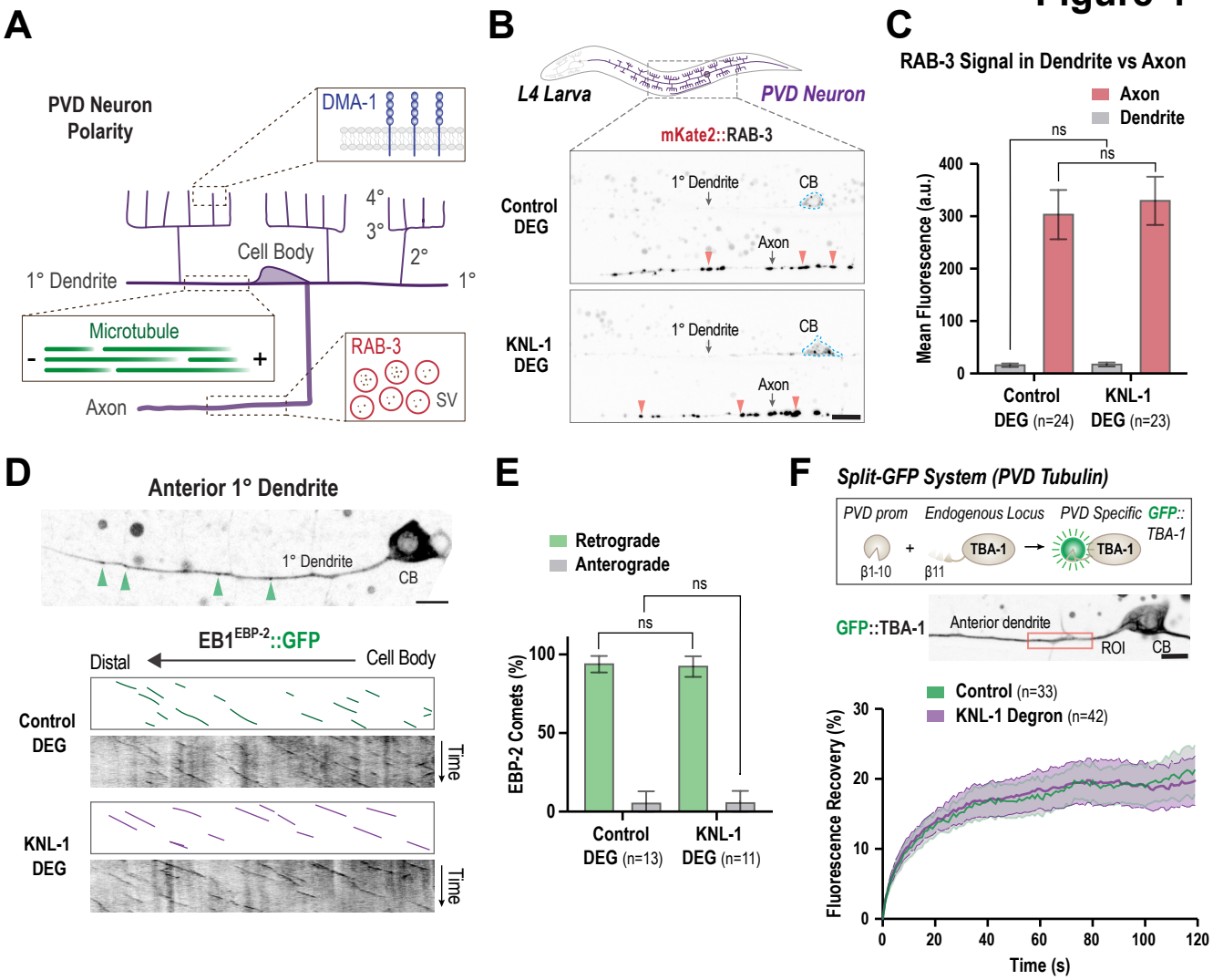
A
PVD Neuron Polarity
DMA-1
4°
3°
2°
Cell Body
1° Dendrite
1°
Microtubule
-
+
RAB-3
SV
Axon
B
L4 Larva
PVD Neuron
mKate2::RAB-3
Control DEG
1° Dendrite
CB
Axon
KNL-1 DEG
1° Dendrite
CB
Axon
C
RAB-3 Signal in Dendrite vs Axon
Axon
Dendrite
ns
ns
Mean Fluorescence (a.u.)
400
300
200
100
0
Control DEG (n=24)
KNL-1 DEG (n=23)
D
Anterior 1° Dendrite
1° Dendrite
CB
EB1EBP-2::GFP
Distal
Cell Body
Control DEG
Time
KNL-1 DEG
Time
E
Retrograde
Anterograde
ns
ns
EBP-2 Comets (%)
100
50
0
Control DEG (n=13)
KNL-1 DEG (n=11)
F
Split-GFP System (PVD Tubulin)
PVD prom
Endogenous Locus
PVD Specific GFP::TBA-1
β1-10
β11
TBA-1
TBA-1
GFP::TBA-1
Anterior dendrite
ROI
CB
Control (n=33)
KNL-1 Degron (n=42)
Fluorescence Recovery (%)
30
20
10
0
0
20
40
60
80
100
120
Time (s)

377 **Figure 4. PVD neuronal polarity & microtubule organization are not affected by post-**
378 **mitotic degradation of KNL-1.**
379 **(A)** Schematic showing DMA-1, the dendrite specific receptor, RAB-3, the synaptic vesicle
380 (SV) marker & the anterior dendrite microtubule organization. **(B)** Localization of the synaptic
381 marker RAB-3 in control & KNL-1 DEG. RAB-3 is enriched in the axon (see red arrowheads).
382 Scale bar, 5μm. **(C)** Quantification of RAB-3 fluorescent signal in the dendrite & axon. **(D)**
383 $EB1^{EBP-2}$::GFP dynamics in the anterior primary dendrite. Plus end comets (arrowhead) are
384 highlighted in the top still image. Below are kymographs projection images of the control (top)
385 & KNL-1 DEG. The kymograph was generated along line extending from cell body towards
386 the distal end of the primary dendrite. Scale bar, 5μm. **(E)** Quantification of $EB1^{EBP-2}$::GFP
387 comet dynamics in control & KNL-1 DEG. **(F)** (Top) Schematic of an endogenous GFP::TBA-
388 1 fusion expressed specifically in PVD using a split-gfp system. (middle) Still image of the
389 anterior primary dendrite that expresses the split-GFP::TBA-1. The red rectangle indicates
390 the Region of Interest (ROI) that was bleached in the FRAP experiments. CB is cell body.
391 Scale bar, 5μm (Bottom) GFP::TBA-1 fluorescence recovery plots for control & KNL-1 DEG.
392

Figure 5

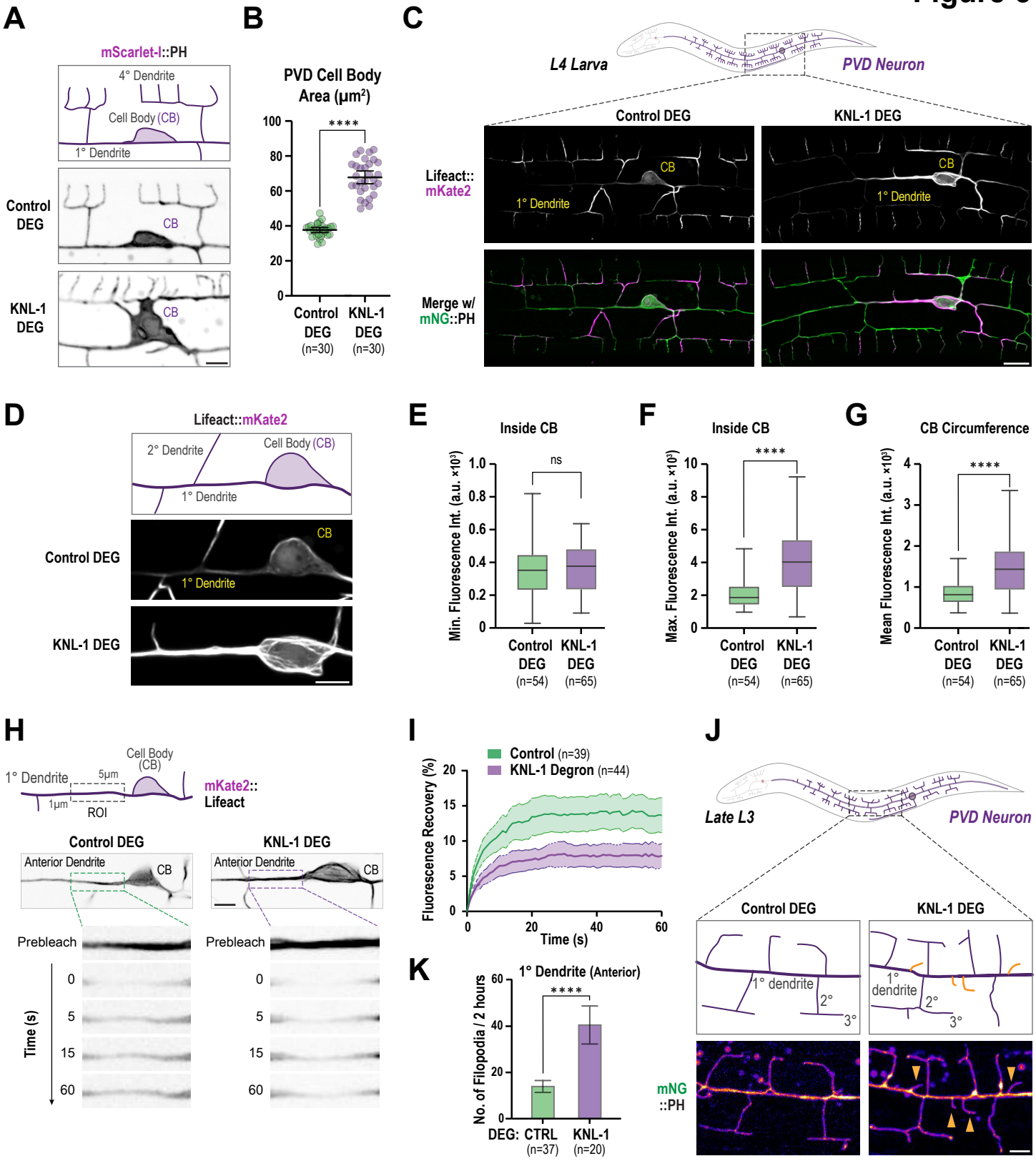
A
mScarlet-I::PH
4° Dendrite
Cell Body (CB)
1° Dendrite
Control DEG
CB
KNL-1 DEG
CB
B
PVD Cell Body Area (μm²)
****
Control DEG (n=30)
KNL-1 DEG (n=30)
C
L4 Larva
PVD Neuron
Control DEG
KNL-1 DEG
Lifeact:: mKate2
CB
1° Dendrite
Merge w/ mNG::PH
D
Lifeact::mKate2
2° Dendrite
Cell Body (CB)
1° Dendrite
Control DEG
KNL-1 DEG
E
Inside CB
ns
Min. Fluorescence Int. (a.u. ×10³)
Control DEG (n=54)
KNL-1 DEG (n=65)
F
Inside CB
****
Max. Fluorescence Int. (a.u. ×10³)
Control DEG (n=54)
KNL-1 DEG (n=65)
G
CB Circumference
****
Mean Fluorescence Int. (a.u. ×10³)
Control DEG (n=54)
KNL-1 DEG (n=65)
H
Cell Body (CB)
1° Dendrite
5μm
1μm
ROI
mKate2:: Lifeact
Control DEG
KNL-1 DEG
Anterior Dendrite
CB
Prebleach
Time (s)
0
5
15
60
I
Control (n=39)
KNL-1 Degron (n=44)
Fluorescence Recovery (%)
Time (s)
J
Late L3
PVD Neuron
Control DEG
KNL-1 DEG
1° dendrite
2°
3°
mNG ::PH
K
1° Dendrite (Anterior)
****
No. of Filopodia / 2 hours
DEG: CTRL (n=37)
KNL-1 (n=20)

393 **Figure 5. The PVD cell body shows an increase in polymerized actin after KNL-1**
394 **degradation.**

395 **(A)** Images of the PVD cell body and proximal regions in control and KNL-DEG. Scale bar,
396 5μm. **(B)** Quantification of the area of the cell body in control & KNL-1 DEG animals. **(C)** The
397 top image shows actin labeled with mKate2::Lifeact while the bottom shows actin overlaid
398 with membrane (mNeonGreen::PH) in control & KNL-1 DEG animals. Scale bar, 10μm. **(D)**
399 Images highlighting actin distribution in the cell body (CB) and proximal anterior primary
400 dendrite in control (top) and KNL-1 DEG (bottom) animals. Scale bar, 5 μm. **(E-G)**
401 Quantification of Lifeact fluorescence intensity inside and on the periphery of the cell body.
402 **(H)** (Top) Still images of the PVD anterior primary dendrite expressing mKate2::Lifeact in
403 control & KNL-1 DEG animals The dashed rectangles indicate the Region of Interests (ROIs)
404 that were bleached in the FRAP experiments. (Bottom) Prebleach and postbleach images of
405 mKate2::Lifeact in control & KNL-1 DEG animals. Scale bar, 5μm. **(I)** mKate2::Lifeact
406 fluorescence recovery plots for control & KNL-1 DEG animals. **(J)** Images of anterior primary
407 dendrite labeled with mNeonGreen::PH in control & KNL-1 DEG late L3 stage animals. Yellow
408 arrowheads indicate filopodia. Scale bar, 5μm. **(K)** Quantification of the filopodial protrusions
409 from anterior primary dendrite during a two-hour time lapse.

Figure 6

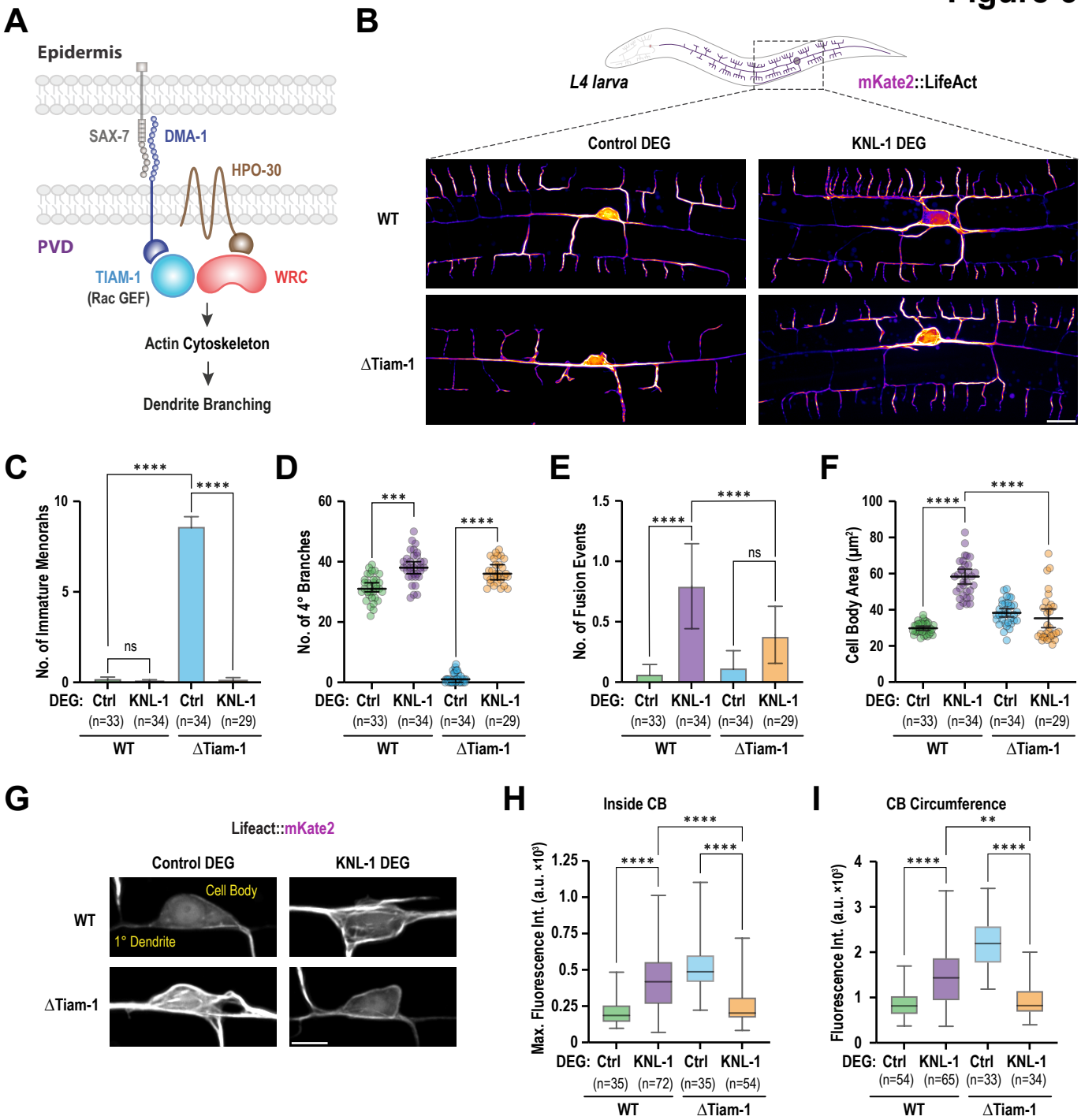
A
Epidermis
SAX-7
DMA-1
HPO-30
PVD
TIAM-1
(Rac GEF)
WRC
Actin Cytoskeleton
Dendrite Branching
B
L4 larva
mKate2::LifeAct
Control DEG
KNL-1 DEG
WT
ΔTiam-1
C
No. of Immature Menorahs
D
No. of 4° Branches
E
No. of Fusion Events
F
Cell Body Area (μm²)
DEG: Ctrl KNL-1 Ctrl KNL-1
(n=33) (n=34) (n=34) (n=29)
WT
ΔTiam-1
G
Lifeact::mKate2
Control DEG
KNL-1 DEG
Cell Body
1° Dendrite
H
Inside CB
Max. Fluorescence Int. (a.u. x10³)
(n=35) (n=72) (n=35) (n=54)
I
CB Circumference
Fluorescence Int. (a.u. x10³)
(n=54) (n=65) (n=33) (n=34)

Figure 6. Degradation of KNL-1 rescues the dendrite branching defects in TIAM-1/RacGEF deletion animals.

410 **(A)** Schematic showing the signaling pathway involved in 3° & 4° dendrite branching.
411 Interactions between the ligand SAX-7 expressed in epidermis and DMA-1 receptor in PVD
412 recruits the TIAM-1/RacGEF which then promotes dendrite branching by activating actin
413 polymerization. **(B)** Images of PVD dendrites expressing mKate2::Lifeact in indicated
414 conditions. Scale bar, 10μm. **(C-E)** Quantification of PVD menorah organization in the
415 indicated conditions. Menorahs that lack 4° branches are considered "immature menorahs".
416 **(F)** Quantification of the area of the cell body in the indicated conditions. **(G)** Images highlight
417 actin distribution in the cell body and proximal anterior primary dendrite in indicated
418 conditions. Scale bar, 5μm. **(H&I)** Quantification of Lifeact fluorescence intensity inside the
419 cell body (CB) in the indicated conditions.

Figure S1

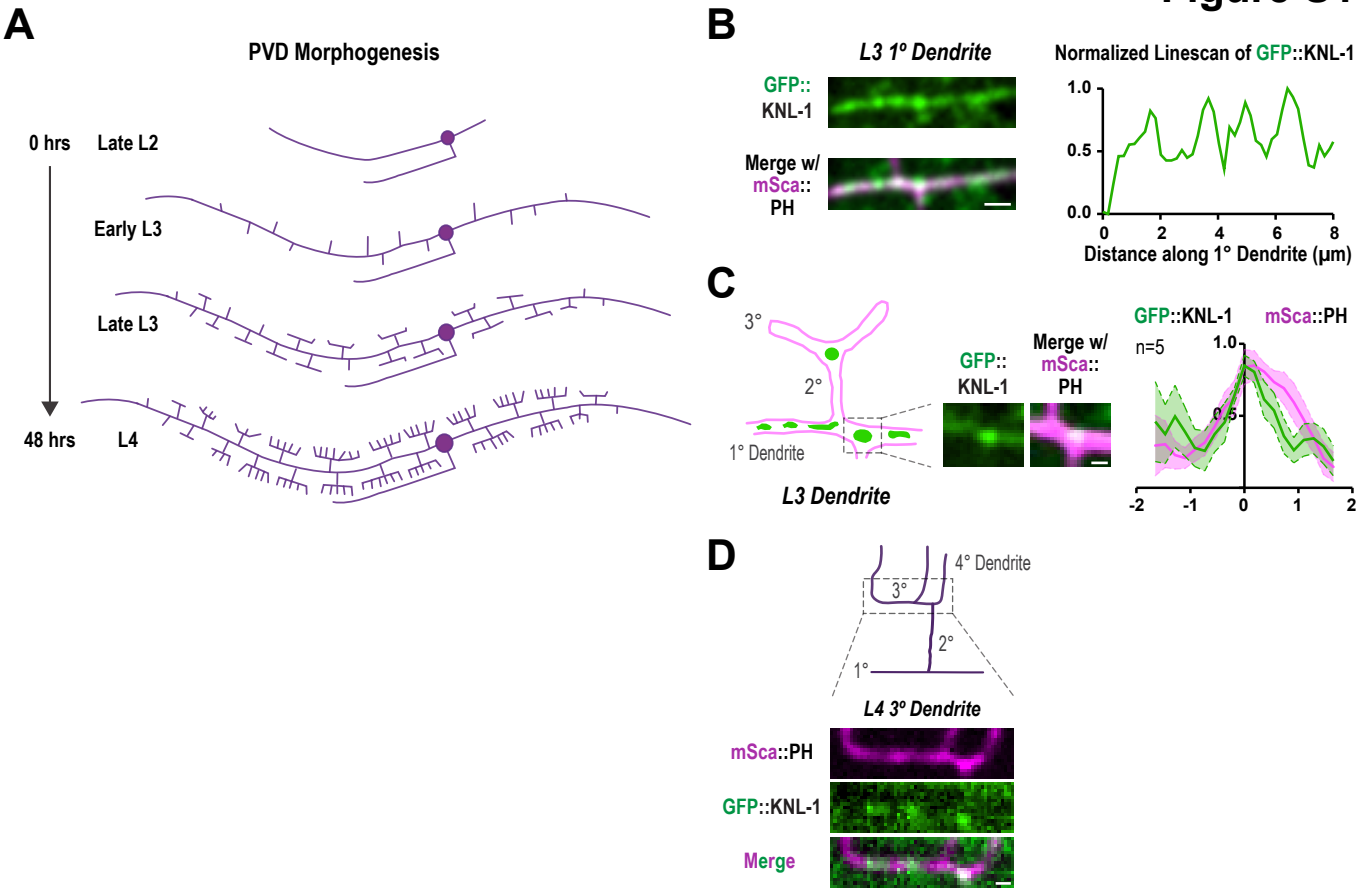
A
PVD Morphogenesis
0 hrs
Late L2
Early L3
Late L3
48 hrs
L4
B
L3 1° Dendrite
GFP::
KNL-1
Merge w/
mSca::
PH
Normalized Linescan of GFP::KNL-1
1.0
0.5
0.0
0
2
4
6
8
Distance along 1° Dendrite (µm)
C
3°
2°
1° Dendrite
L3 Dendrite
GFP::
KNL-1
Merge w/
mSca::
PH
GFP::KNL-1
mSca::PH
n=5
1.0
0.5
-2
-1
0
1
2
D
4° Dendrite
3°
2°
1°
L4 3° Dendrite
mSca::PH
GFP::KNL-1
Merge

Figure S1. PVD morphogenesis & KNL-1 localization.

420 **(A)** Schematic of the PVD neuron morphogenesis from L2 stage until the L4 larval stage.
421 Dendrite outgrowth, branching and menorah formation takes about 48 hours. **(B)** (Left)
422 Localization of GFP::KNL-1 within the primary dendrite at the L3 stage. KNL-1 forms distinct
423 puncta like structures. Scale bar, 2 μm. (Right) Linescan of the GFP::KNL-1 intensity. The
424 peaks correspond to the puncta seen on the image. **(C)** (Left) Schematic and image
425 showing GFP::KNL-1 enrichment at the base of branchpoint between 1° and 2° dendrite at
426 the L3 stage. Scale bar, 1 μm. (Right) Plot showing the average of the fluorescent intensity
427 linescans of GFP::KNL-1 superimposed with that of mScarlet-I::PH. Branchpoints show an
428 increased intensity of PH and KNL-1 signal. **(D)** Image shows distribution of GFP::KNL-1
429 within the 3° dendrite at the early L4 stage. Scale bar, 2 μm.

Figure S2

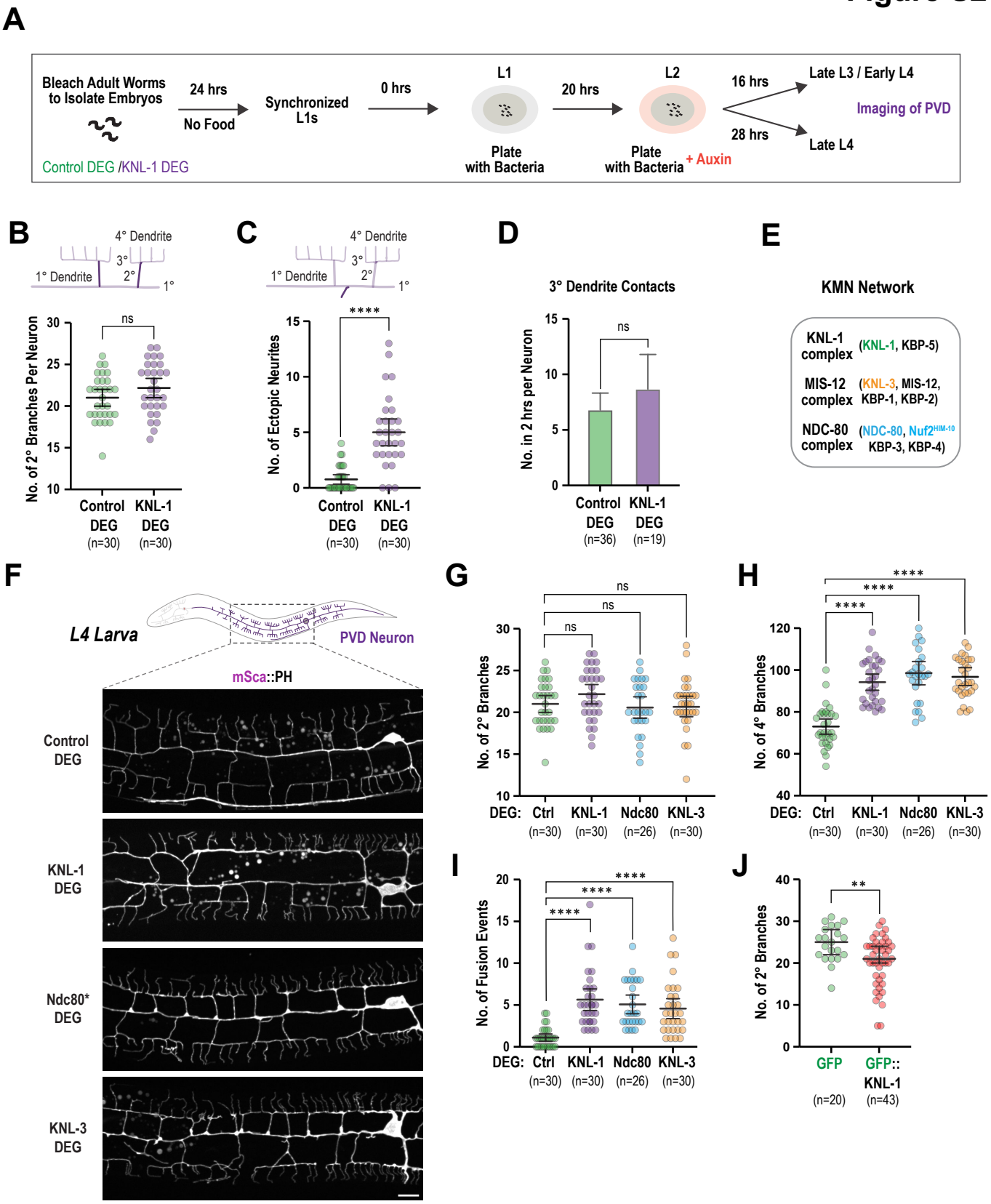
A
Bleach Adult Worms to Isolate Embryos
24 hrs
No Food
Synchronized L1s
0 hrs
L1
Plate with Bacteria
20 hrs
L2
Plate with Bacteria
+ Auxin
16 hrs
Late L3 / Early L4
Imaging of PVD
28 hrs
Late L4
Control DEG /KNL-1 DEG
B
4° Dendrite
3°
1° Dendrite
2°
1°
No. of 2° Branches Per Neuron
ns
Control DEG (n=30)
KNL-1 DEG (n=30)
C
No. of Ectopic Neurites
****
Control DEG (n=30)
KNL-1 DEG (n=30)
D
3° Dendrite Contacts
No. in 2 hrs per Neuron
ns
Control DEG (n=36)
KNL-1 DEG (n=19)
E
KMN Network
KNL-1 complex (KNL-1, KBP-5)
MIS-12 complex (KNL-3, MIS-12, KBP-1, KBP-2)
NDC-80 complex (NDC-80, Nuf2HIM-10 KBP-3, KBP-4)
F
L4 Larva
PVD Neuron
mSca::PH
Control DEG
KNL-1 DEG
Ndc80* DEG
KNL-3 DEG
G
No. of 2° Branches
ns
DEG: Ctrl (n=30) KNL-1 (n=30) Ndc80 (n=26) KNL-3 (n=30)
H
No. of 4° Branches
****
DEG: Ctrl (n=30) KNL-1 (n=30) Ndc80 (n=26) KNL-3 (n=30)
I
No. of Fusion Events
****
DEG: Ctrl (n=30) KNL-1 (n=30) Ndc80 (n=26) KNL-3 (n=30)
J
No. of 2° Branches
**
GFP (n=20)
GFP:: KNL-1 (n=43)

Figure S2. Effects of degradation of KMN network on PVD morphology.

430 **(A)** Schematic indicates the experimental design for degrading AID::KNL-1. To obtain
431 synchronized L1 animals, embryos from control or AID::KNL-1 adult worms expressing PVD-
432 specific TIR1 transgene were isolated by bleach treatment and hatched for 24 hours on plates
433 without food. L1 larvae were placed on a plate with food until they reached the L2 stage
434 (20hrs). The L2 stage animals were transferred to plates with bacteria and auxin and grown
435 until they reached L4 stage (24hrs). The late L4 stage animals have fully developed menorahs
436 and were imaged to analyze the PVD morphology. **(B&C)** Quantification of the numbers of 2°
437 branches and the number of ectopic branches in control & KNL-1 DEG. **(D)** Quantification of
438 the filopodial protrusions from the anterior primary dendrite during two-hour time lapses. **(E)**
439 Schematic of the components of the KNL1/Mis12/Ndc80 complex. **(F)** Images of PVD
440 dendrite organization in control, KNL-1 DEG, Ndc80 DEG & KNL-3 DEG.* In the Ndc80 DEG,
441 AID was fused to both NDC-80 & NUF2$^{Him1-10}$ subunits. Scale bar, 10 μm. **(G-I)** Quantification
442 of PVD dendrite organization including the number of 2° & 4° branches and fusions between
443 menorahs in the indicated conditions. **(J)** Quantification of the number of 2° branches in the
444 dendrites of PVD in control and KNL-1::GFP overexpressing animals.

Figure S3

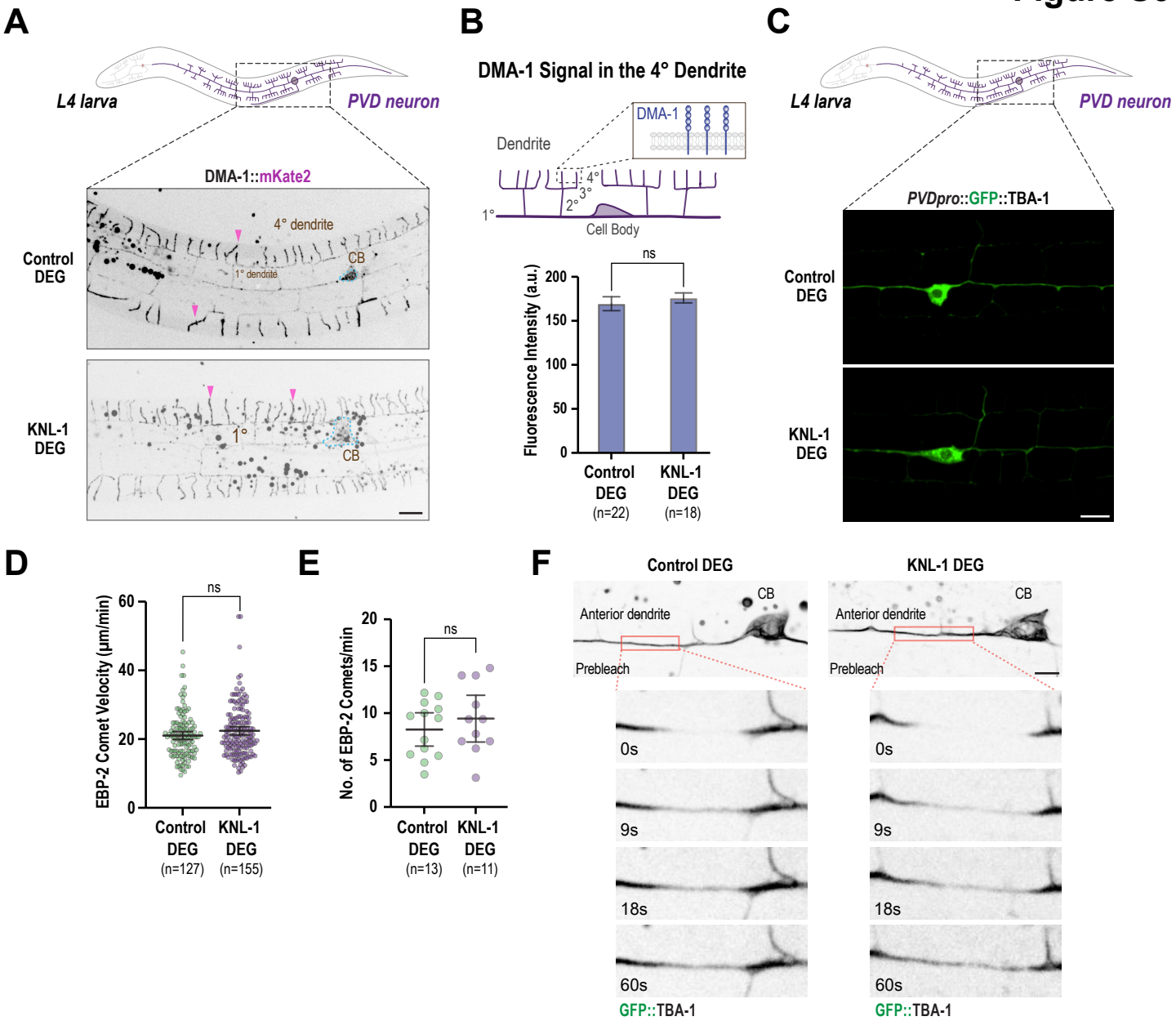
A
L4 larva
PVD neuron
DMA-1::mKate2
Control DEG
KNL-1 DEG
4° dendrite
1° dendrite
CB
1°
B
DMA-1 Signal in the 4° Dendrite
Dendrite
DMA-1
4°
3°
2°
1°
Cell Body
Fluorescence Intensity (a.u.)
ns
Control DEG (n=22)
KNL-1 DEG (n=18)
C
L4 larva
PVD neuron
PVDpro::GFP::TBA-1
Control DEG
KNL-1 DEG
D
EBP-2 Comet Velocity (µm/min)
ns
Control DEG (n=127)
KNL-1 DEG (n=155)
E
No. of EBP-2 Comets/min
ns
Control DEG (n=13)
KNL-1 DEG (n=11)
F
Control DEG
KNL-1 DEG
Anterior dendrite
CB
Prebleach
0s
9s
18s
60s
GFP::TBA-1

Figure S3. DMA-1 distribution & microtubule organization & stability after degradation of KNL-1 in the PVD.

445 **(A)** Localization of the dendrite guidance receptor, DMA-1 in control & KNL-1 DEG at the L4
446 stage. Pink arrow heads show enrichment of DMA-1 in the 4° dendrite. Scale bar, 10μm.
447 DMA-1 is restricted to dendrite structures and no axonal signal for DMA-1 is visible **(B)**
448 Quantification of DMA-1 fluorescent signal in the PVD dendrites shows that both the control
449 and KNL-1 has similar levels of DMA-1. **(C)** Images of Pdes-2 driven GFP::TBA-1 in the
450 control & KNL-1 degrader animals. Tubulin distribution looks similar in both conditions.
451 GFP::TBA-1 is detected predominantly in the 1° dendrite and is largely absent from the
452 dendrite branches. Scale bar, 10 μm. **(D&E)** Quantification of $EB1^{EBP-2}$::GFP comet dynamics
453 in control & KNL-1 DEG. **(F)** (Top) Still images of the PVD anterior primary dendrite
454 expressing endogenous GFP::TBA-1 in control & KNL-1 DEG animals. Scale bar, 5 μm. The
455 dashed rectangles indicate the Region of Interest (ROI) that were bleached in the FRAP
456 experiments. (Bottom) Prebleach and postbleach images of GFP::TBA-1 in control & KNL-1
457 DEG animals.

Figure S4

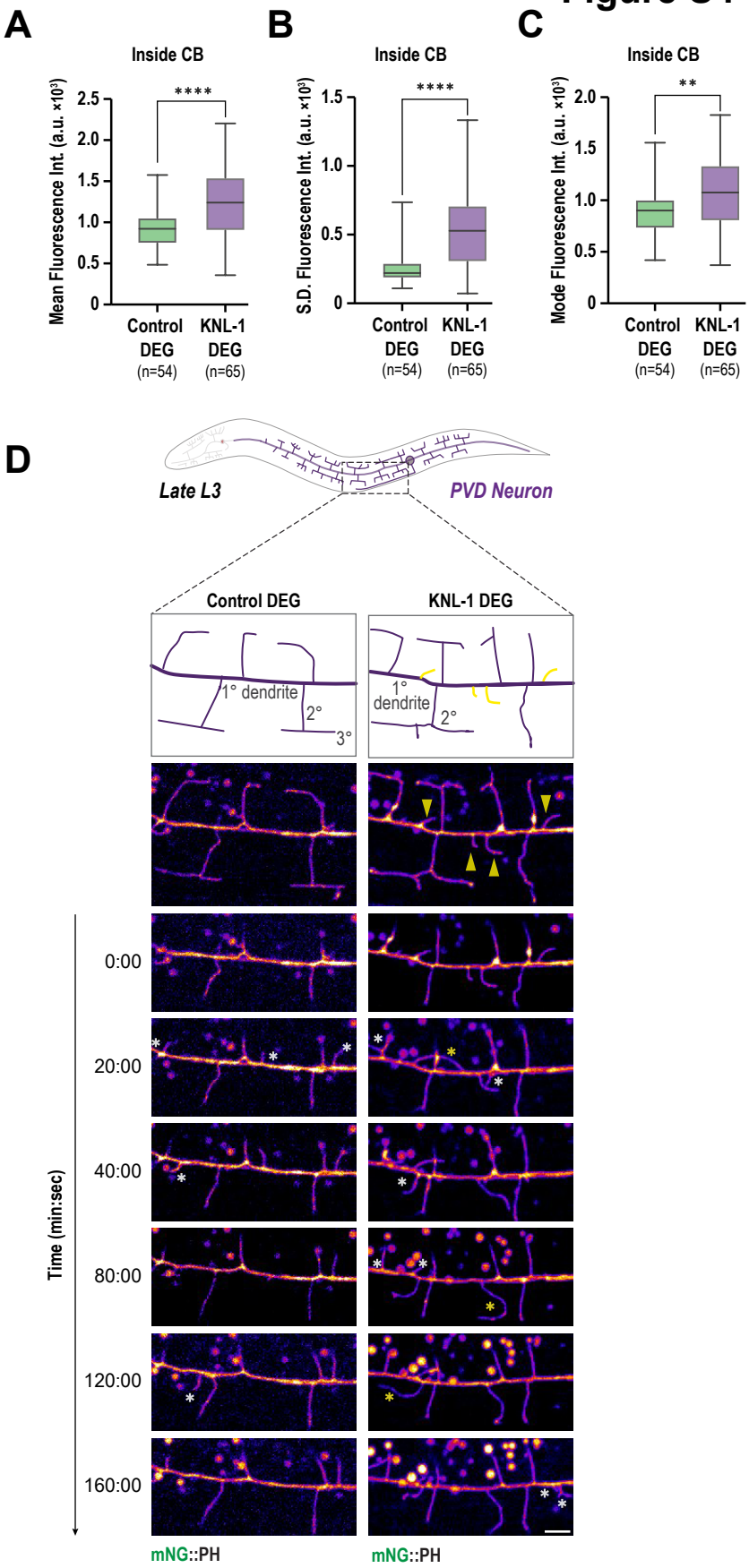
A
Inside CB
Mean Fluorescence Int. (a.u. ×10³)
2.5
2.0
1.5
1.0
0.5
0
****
Control DEG (n=54)
KNL-1 DEG (n=65)
B
Inside CB
S.D. Fluorescence Int. (a.u. ×10³)
1.5
1.0
0.5
0
****
Control DEG (n=54)
KNL-1 DEG (n=65)
C
Inside CB
Mode Fluorescence Int. (a.u. ×10³)
2.0
1.5
1.0
0.5
0
**
Control DEG (n=54)
KNL-1 DEG (n=65)
D
Late L3
PVD Neuron
Control DEG
KNL-1 DEG
1° dendrite
2°
3°
1° dendrite
2°
Time (min:sec)
0:00
20:00
40:00
80:00
120:00
160:00
mNG::PH
mNG::PH

Figure S4. Analysis of F-actin distribution of in the control and KNL-1 degraded animals; filopodia dynamics in L3 animals.

458 **(A-C)** Quantification of Lifeact fluorescence intensity inside the cell body. **(D)** Snapshots of
459 time lapse imaging of 1° dendrite branch dynamics in control & KNL-1 DEG animals at the
460 late L3 stage. Yellow arrowheads indicate filopodia. White asterisks indicate newly formed
461 filopodia. Yellow asterisks indicate the misguided filopodia that runs parallel to the 1° dendrite.
462 Scale bar, 5 μm

Figure S5

A

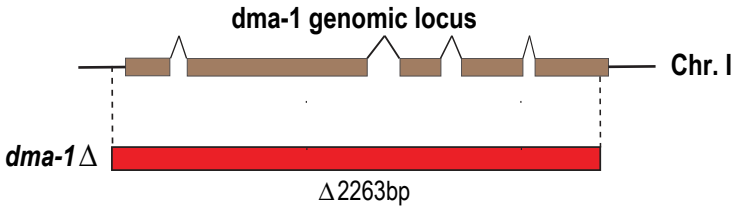
dma-1 genomic locus
Chr. I
dma-1Δ
Δ2263bp

B

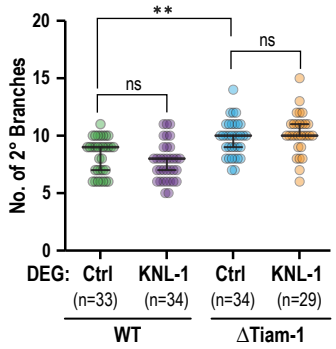
No. of 2° Branches
20
15
10
5
0
**
ns
ns
DEG:
Ctrl
KNL-1
Ctrl
KNL-1
(n=33)
(n=34)
(n=34)
(n=29)
WT
ΔTiam-1

Figure S5. Analysis of KNL-1 degradation in dma-1 and tiam-1 deletion background.

463 **(A)** Schematic of the dma-1 gene deletion. Dashed line point to the location of the crRNAs
464 that were used to generate the gene deletion. **(B)** Quantification of PVD 2° branches in the
465 indicated conditions. tiam-1Δ shows a slight increase in the number of 2° branches. As the
466 counts are from a single timepoint it is not clear whether these are stable 2° branches or long
467 unstable filopodia.

MATERIALS AND METHODS

C. elegans Strains & Methods

468 All *C. elegans* strains were maintained at 20°C on standard Nematode Growth Media
469 (NGM) plates seeded with OP50 bacteria. The genotypes of the *C. elegans* strains used in
470 this study are described in *Table S1*.
471 Single copy transgenic integrations were engineered using the transposon based mos1
472 mediated Single Copy Insertion (mosSCI) method[40]. Briefly, the strains were generated by
473 injecting a mixture of repair plasmid containing the transgene and a positive selection marker,
474 transposase plasmid, and the three plasmids encoding fluorescent markers for negative
475 selection [pCFJ90 (P*myo-2::mCherry*), pCFJ104 (P*myo-3::mCherry*) and pGH8 (P*rab-*
476 *3::mCherry*)] into appropriate *C. elegans* strains that contain mos1 insertion sites at specific
477 genomic locations within Chr I, II, IV or V. Positive integrants were identified by selecting
478 worms that were moving and did not contain fluorescent selection markers. Integration of
479 transgenes were confirmed by PCR, spanning both homology arms. Endogenous tagging of
480 various genes (see *Table S1*) at the N- or C-teminus and generation of the *dma-1* deletion
481 were done using CRISPR/Cas9 methods [41–43]. The specific method and guide RNAs used to
482 generate each strain are described in *Table S2*. Briefly, a DNA mix (Dickinson et al., 2015;
483 Waaijers et al., 2013) or Cas9RNP mix (Paix et al., 2015), containing the respective repair
484 template, guide RNA sequences, Cas9 and selection markers were injected into N2 animals.
485 Recombinant strains were identified by appropriate selection method and were confirmed by
486 PCR, spanning both homology regions. All plasmids used for the strain constructions were
487 constructed using the Gibson Assembly method [44].

Auxin Degradation

488 Worms were synchronized at L1 arrest stage by bleaching gravid adults in NGM plate
489 using a 1M sodium hydroxide and 2.5% sodium hypochlorite (Acros Organics) solution to
490 obtain eggs. The eggs were then left to hatch for 48 hours at 20°C allow hatched L1 larvae
491 to enter L1 arrest stage. Subsequently, the worms were washed with M9 buffer and
492 transferred into a centrifuge tube for pelleting for 1 min at 1000 RPM. The pelleted
493 synchronized L1s were transferred to OP-50 seeded NGM plates and maintained at 20°C
494 (T=0hr). Auxin treatment was performed by transferring worms to OP-50 seeded NGM plates
495 containing 4 mM auxin (K-NAA, N160, Phytochrome laboratories) at T=20hr post
496 synchronization. The auxin containing NGM plates were seeded with 200μl of high-density
497 OP-50 and left to dry for 2 days at room temperature. The seeded plates were stored for up
498 to 1 month at 4°C.

Fluorescence microscopy and image analysis

499 To image PVD neurons expressing the appropriate markers L2 or L4 stage worms
500 were anaesthetized in 5 mM Levamisole and mounted in M9 on a 2% agarose pad. Images
501 were acquired using a spinning disc confocal imaging system with a Yokogawa spinning disk
502 unit (CSU-W1), a Nikon Ti2-E fully motorized inverted microscope, with a CFI60 Plan
503 Apochromat lambda 60X Oil (Nikon) objective and a Photometrics Prime 95B camera. For
504 imaging Lifeact::mKate2 marker a CFI60 Plan Apochromat lambda 100X Oil (Nikon) objective
505 was used. Z-stacks of 0.5 μm or 1.0 μm were acquired to cover the PVD closer to the side
506 facing the coverslip / objective.

507 To quantify KNL-1 degradation the Z-stacks were projected into a maximum intensity
508 projection. The mean intensity of KNL-1::GFP at the cell body was measured using a polygon
509 selection drawn over the cell body boundary using Image J (Fiji).
510 To quantify co-localization of mSca::PH with KNL1::GFP separate line scans were
511 acquire using a segmented line (width=1 pixels) at a maximum of 2 μm of either side of the
512 branchpoint/base of the branch using Image J (Fiji). The values were normalized to the
513 maximum and minimum intensity value.
514 To quantify the morphology of the PVD dendrites the Z-stacks were projected into a
515 maximum intensity projection. The various dendrite morphology parameters were measured
516 separately for the posterior dendrite and the anterior proximal dendrite (100μm & 50 μm from
517 the soma for worms expressing the PH marker & Lifeact marker, respectively). The 2°
518 dendrites were identified as orthogonal branches to 1^odendrite containing higher order
519 branches (3° and/or 4° branches). The 4° dendrites were identified as orthogonal branches to
520 the 3^odendrites. Fusion was identified as two adjacent 3° dendrite lacking a gap (Smith et al.,
521 2012). Ectopic branches were identified as branches protruding out of the 1° dendrite with a
522 length of at least 2x higher than its width and with no higher order branches. The cell body
523 area was measured using a polygon selection drawn over the cell body boundary using Image
524 J (Fiji).
525 To quantify the morphology of the PVD dendrites for the extrachromosomal arrays the
526 fluorescence intensity of GFP or KNL-1::GFP were measured in the cell body using the
527 polygon selection drawn over the cell body boundary using Image J (Fiji). The values were
528 normalised to the background fluorescence intensity to ensure only worms with over-
529 expression were included in the analysis. Hence, if the intensity was greater than half the

530 max recorded intensity then the worms were included in the analysis. The morphology was
531 quantified for the whole neuron using the parameters previously described.

532 To quantify RAB-3 signal the Z-stacks were projected into a maximum intensity
533 projection and the fluorescence intensity was measured along the length of the axon of each
534 neuron and along an equivalent length in the proximal anterior dendrite using a segmented
535 line (width=3 pixels) in Image J (Fiji). To quantify DMA-1 signal the Z-stacks were projected
536 into a maximum intensity projection and the fluorescence intensity was measured in the 4°
537 dendrites adjacent to the cell body using a segmented line (width=3 pixels) in Image J (Fiji).

538 To quantify actin distribution at the cell body the Z-stacks were projected into a
539 maximum intensity projection of the z-planes that included one single PVD neuron (~18 x 1
540 µm z-stacks). Mean intensity of actin around the cell body was measured using a segmented
541 line (width=3 pixels) drawn over the cell body boundary with the anterior side as the start
542 point and following a clockwise direction using Image J (Fiji). The standard deviation,
543 maximum and minimum intensity of actin at the cell body were measured using a polygon
544 selection drawn over the cell body boundary using Image J (Fiji).

545 To quantify membrane blebbing in L4 worms the Z-stacks were projected into a
546 maximum intensity projection and membrane blebbing was quantified for the whole anterior
547 dendrite.

548 To quantify LGG-1 puncta in day 3 adults, the Z-stacks were projected into a
549 maximum intensity projection and a 50 µm x 50 µm section centred around the cell body
550 was analysed for each worm. LGG-1 puncta were counted if they were not in the cell body
551 or axon initial segment.

Timelapse Imaging

552 For time-lapse imaging of dendrite dynamics, synchronized worms were anesthetized
553 in 5 mM Levamisole after auxin treatment at 8 hours post synchronization or in the absence
554 of treatment. 9-11 x 0.9 µm z-stacks were acquired at 1 frame per 1:20 minutes for 2 hours
555 and an exposure of 50 ms. Acquisition was performed using using a spinning disc confocal
556 imaging system with a Yokogawa spinning disk unit (CSU-W1), a Nikon Ti2-E fully motorized
557 inverted microscope, with a CFI60 Plan Apochromat lambda 60X Oil (Nikon) objective and
558 Photometrics Prime 95B camera.

559 For quantifications, time of contact of 3° dendrites, number of contacts and number of
560 unresolved of contacts were measured from maximum intensity projections of z-stacks using
561 Image J (Fiji). This quantification was performed for the first 100 µm anterior to the soma.
562 Contacts of 3° dendrites were identified as two adjacent 3° dendrite lacking a gap (Smith et
563 al., 2012). Only the contacts that occurred during the timelapse acquisition were quantified.
564 Unresolved contacts were identified as contacts that lacked a gap by the end of the
565 timelapses. Protrusions were identified as any membrane protrusions smaller than 2.5 µm.

566 For timelapse imaging of EBP-2 dynamics synchronized worms were anesthetized in
567 5 mM Levamisole after auxin treatment. A single z-slice was acquired of the first 50 µm of the
568 anterior dendrite at 1 frame per 1 sec using a spinning disc confocal imaging system with a
569 Yokogawa spinning disk unit (CSU-W1), a Nikon Ti2-E fully motorized inverted microscope,
570 with a CFI60 Plan Apochromat lambda 100X Oil (Nikon) objective and an Photometrics Prime
571 95B camera. For the generation of kymographs Fiji plugin, KymographClear 2.0a[45] was
572 used. A line of width 2 pixel was drawn to generate kymograph. The number of
573 lines (indicative of the number of comets) in each direction was measured and the length and
574 height of each line was used to calculate the velocities of each individual comet.

Fluorescence Recovery After Photobleaching (FRAP) of Actin and Microtubule

575 For FRAP imaging of microtubule marker worms were anesthetized in 5 mM
576 Levamisole. A single z-slice was acquired of the first 50 µm of the anterior dendrite at 1 frame
577 per 1 sec. After 3 prebleach frames, 1.5 µm region 20 µm away from the cell body was
578 bleached using 405 nm laser at 30% power, 150 µs dwell time and 5 laser iterations. Images
579 were acquired for 2 minutes post bleaching. For FRAP imaging of actin marker worms were
580 anesthetized in 5 µl 5mM Levamisole in M9. A single z-slice was acquired of the first 50 µm
581 of the anterior dendrite at 1 frame per 1 sec and an exposure of 150 ms. After 3 prebleach
582 frames, 1.5 µm region 20 µm away from the cell body was bleached using 405 nm laser at
583 40% power, 300 µs. Dwell time and 5 laser iterations. Images were acquired for 2 minutes
584 post bleaching.

585 To quantify fluorescence intensity a region of interest (ROI) of 1.5 µm was defined
586 using elliptical selection in Image J (Fiji). The fluorescence intensity was normalized to the
587 background and corrected for the fluorescence intensity of non-bleached area. Additionally,
588 the FRAP actin marker analysis required the values to be additionally subtracted by the
589 intensity at the photobleached region 1 frame post photobleaching.

Behavioural assays

590 For the locomotion assays L4 worms were transferred to a freshly seeded NGM plate
591 for 1 hour at 20°C after auxin treatment. Acquisition was performed using Nikon SMZ18
592 microscope at 2X P2-SHR Plan Apo 1X objective and Photometrics Cool SNAP camera. 5
593 tracks were measured per worm and 15 worms were measured per strain. The wavelength
594 was measured as the distance between two successive peaks and the amplitude as half the

measurement of the height between two opposing peaks. Five measurements were taken per track.

Quantification and Statistical Analysis

Details of the methods employed to extract and quantify various parameters in microscopy datasets are described in the image analysis section. The statistical tests used to determine significance are described in the figure legends. The data normality was assessed using a Shapiro-Wilk test. For normally distributed data either an unpaired t-test (for comparisons between two groups) or an ordinary one-way ANOVA with a follow up Holm-Sidak multiple comparison test (for comparisons between three and more groups) were performed. For data sets that did not pass the normality test either a Mann-Whitney test (for comparisons between two groups) or a Kruskal-Wallis test with a follow up Dunn's multiple comparison test (for comparisons between three and more groups) were performed. All comparisons were done in GraphPad Prism (GraphPad Software) and the stars ****, ***, ** and ns correspond $p<0.0001$, $p<0.001$, $p<0.01$ and "not significant", respectively.

Table S1. *C. elegans* Strains

STRAIN DESCRIPTION	SOURCE	IDENTIFIER
dhaSI145 [oxTi185; pDC973; Pdes-2--TIR1--F2A--mTagBFP--AID--NLS--tbb-23'UTR; cb-unc-119(+)]I #1; dhaSi89 [pDC747; Punc-86::TIR-1::unc543'UTR; cb-unc-119(+)]II #1; ; unc-119(ed3)III?; dhaSi76[oxTi177;PDC731; Pdes-2::mSca-PH::unc-54 3'UTR; cb-unc-119(+)] IV*	This study	DKC815
dhaSI145 [oxTi185; pDC973; Pdes-2--TIR1--F2A--mTagBFP--AID--NLS--tbb-23'UTR; cb-unc-119(+)]I #1; dhaSi89 [pDC747; Punc-86::TIR-1::unc543'UTR; cb-unc-119(+)]II #1; knl-1(dha122 (AID::dTagmB>F>P::::KNL-1))III ; unc-119(ed3)III?; dhaSi76[oxTi177;PDC731; Pdes-2::mSca-PH::unc-54 3'UTR; cb-unc-119(+)] IV*	This study	DKC849
dhaSI145 [oxTi185; pDC973; Pdes-2--TIR1--F2A--mTagBFP--AID--NLS--tbb-23'UTR; cb-unc-119(+)]I #1; dhaSi89 [pDC747; Punc-86::TIR-1::unc543'UTR; cb-unc-119(+)]II #1; ; dhaSi76[ndc-80(dha148; NDC-80::AID::dgfp^3XFLAG) ; oxTi177;PDC731; Pdes-2::mSca-PH::unc-54 3'UTR; cb-unc-119(+)] IV dhaSi76[oxTi177;PDC731; Pdes-2::mSca-PH::unc-54 3'UTR; cb-unc-119(+)] IV*	This study	DKC860
dhaSI145 [oxTi185; pDC973; Pdes-2--TIR1--F2A--mTagBFP--AID--NLS--tbb-23'UTR; cb-unc-119(+)]I #1; dhaSi89 [pDC747; Punc-86::TIR-1::unc543'UTR; cb-unc-119(+)]II #1; unc-119(ed3)III?; dhaSi76[oxTi177;PDC731; Pdes-2::mSca-PH::unc-54 3'UTR; cb-unc-119(+)] IV; KNL-3(du2 [AID::KNL-3]) V*	This study	DKC911
dhaEx1[Pdes-2::Knl-1::GFP::unc 54 3'UTR]; dhaSi76[oxTi177;PDC731; Pdes-2::mSca-PH::unc-54 3'UTR; cb-unc-119(+)] IV	This study	DKC822
dhaEx3[Pdes-2::GFP::unc 54 3'UTR]; dhaSi76[oxTi177;PDC731; Pdes-2::mSca-PH::unc-54 3'UTR; cb-unc-119(+)] IV	This study	DKC824
dhaSI145 [oxTi185; pDC973; Pdes-2--TIR1--F2A--mTagBFP--AID--NLS--tbb-23'UTR; cb-unc-119(+)]I #1; dhaSi89 [pDC747; Punc-86::TIR-1::unc543'UTR; cb-unc-119(+)]II #1; knl-1(dha122 (AID::dTagmB>F>P::::KNL-1))III ; unc-119(ed3)III?; hrtSi17[Pdes-2::mKate2::rab-3 LG]IV*	This study	DKC1002
dhaSI145 [oxTi185; pDC973; Pdes-2--TIR1--F2A--mTagBFP--AID--NLS--tbb-23'UTR; cb-unc-119(+)]I #1; dhaSi89 [pDC747; Punc-86::TIR-1::unc543'UTR; cb-unc-119(+)]II #1; unc-119(ed3)III?; hrtSi17[Pdes-2::mKate2::rab-3 LG]IV*	This study	DKC1001
dhaSI145 [oxTi185; pDC973; Pdes-2--TIR1--F2A--mTagBFP--AID--NLS--tbb-23'UTR; cb-unc-119(+)]I #1; dhaSi89 [pDC747; Punc-86::TIR-1::unc543'UTR; cb-unc-119(+)]II #1; dhaSi272[oxTi177; pDC1122 ;Pser2-prom-3::DMA-1::mKate2::unc 54 3'UTR ; cb-unc-119(+)]V*	This study	DKC1076
dhaSI145 [oxTi185; pDC973; Pdes-2--TIR1--F2A--mTagBFP--AID--NLS--tbb-23'UTR; cb-unc-119(+)]I #1; dhaSi89 [pDC747; Punc-86::TIR-1::unc543'UTR; cb-unc-119(+)]II #1; knl-1(dha122 (AID::dTagmB>F>P::::KNL-1))III ; unc-119(ed3)III?; dhaSi272[oxTi177; pDC1122 ;Pser2-prom-3::DMA-1::mKate2::unc 54 3'UTR ; cb-unc-119(+)]V*	This study	DKC1075
dhaSI145 [oxTi185; pDC973; Pdes-2--TIR1--F2A--mTagBFP--AID--NLS--tbb-23'UTR; cb-unc-119(+)]I #1; dhaSi89 [pDC747; Punc-86::TIR-1::unc543'UTR; cb-unc-119(+)]II #1; dhaSi76[oxTi177;PDC731; Pdes-2::mSca-PH::unc-54 3'UTR; cb-unc-119(+)] IV; dhaSi241[oxTi177;PDC978; Pdes-2::GFP::tba-1::unc-54-3'UTR; cb-unc-119(+)] V #1*	This study	DKC917

dhaSI145 [oxTi185; pDC973; Pdes-2--TIR1--F2A--mTagBFP--AID--NLS--tbb-23'UTR; cb-unc-119(+)]I #1; dhaSi89 [pDC747; Punc-86::TIR-1::unc543'UTR; cb-unc-119(+)]II #1; knl-1(dha122 (AID::dTagmB>F>P::::KNL-1))III ; unc-119(ed3)III?; dhaSi76[oxTi177;PDC731; Pdes-2::mSca-PH::unc-54 3'UTR; cb-unc-119(+)] IV; dhaSi241[oxTi177;PDC978; Pdes-2::GFP::tba-1::unc-54-3'UTR; cb-unc-119(+)] V #1*	This study	DKC916
dhaSI145 [oxTi185; pDC973; Pdes-2--TIR1--F2A--mTagBFP--AID--NLS--tbb-23'UTR; cb-unc-119(+)]I #1; dhaSi89 [pDC747; Punc-86::TIR-1::unc543'UTR; cb-unc-119(+)]II #1; knl-1(dha122 (AID::dTagmB>F>P::::KNL-1))III; dhaSi45[oxTi365; pDC675; Pdes-2::mNG-PH::unc-54 3'UTR; cb-unc-119(+)] V clone A*	This study	DKC1089
dhaSi89 [pDC747; Punc-86::TIR-1::unc543'UTR; cb-unc-119(+)]II #1; knl-1(dha130; HA::7XGFP11::knl-1)III; dhaSi76[oxTi177;PDC731; Pdes-2::mSca-PH::unc-54 3'UTR; cb-unc-119(+)] IV ;outcrossed 3X ; dhaSi207 [pDC1020;unc-86pro::splitGFP1-10::tbb-2 3'UTR; cb-unc-119(+)] V #2	This study	DKC1139
dhaSi89 [pDC747; Punc-86::TIR-1::unc543'UTR; cb-unc-119(+)]II #1; knl-1(dha185; HA::7XGFP11::knl-1::AID)III; dhaSi76[oxTi177;PDC731; Pdes-2::mSca-PH::unc-54 3'UTR; cb-unc-119(+)] IV ;outcrossed 3X ; dhaSi207 [pDC1020;unc-86pro::splitGFP1-10::tbb-2 3'UTR; cb-unc-119(+)] V	This study	DKC1151
dhaSi207 [pDC1020;unc-86pro::splitGFP1-10::tbb-2 3'UTR; cb-unc-119(+)] II #2; knl-1(dha130; HA::7XGFP11::knl-1)III unc-119(ed3)III; dhaSi76[oxTi177;PDC731; Pdes-2::mSca-PH::unc-54 3'UTR; cb-unc-119(+)] IV ;outcrossed 3X	This study	DKC870
dhaSi249 [oxTi177; pDC732 Punc-86::mSca-PH::unc-54 3'UTR] V #1; dhaSi207 [pDC1020;unc-86pro::splitGFP1-10::tbb-2 3'UTR; cb-unc-119(+)] II #2; knl-1(dha130; HA::7XGFP11::knl-1)III	This study	DKC872
dhaSI145 [oxTi185; pDC973; Pdes-2--TIR1--F2A--mTagBFP--AID--NLS--tbb-23'UTR; cb-unc-119(+)]I #1; dhaSi89 [pDC747; Punc-86::TIR-1::unc543'UTR; cb-unc-119(+)]II #1; dhaSi243[pDC929; oxTi365; Pdes-2--LifeAct-mKate2--tbb-2 3UTR; cb-unc-119(+)]IV #1*	This study	DKC1035
dhaSI145 [oxTi185; pDC973; Pdes-2--TIR1--F2A--mTagBFP--AID--NLS--tbb-23'UTR; cb-unc-119(+)]I #1; dhaSi89 [pDC747; Punc-86::TIR-1::unc543'UTR; cb-unc-119(+)]II #1; knl-1(dha122 (AID::dTagmB>F>P::::KNL-1))III ; unc-119(ed3)III?; dhaSi243[pDC929; oxTi365; Pdes-2--LifeAct-mKate2--tbb-2 3UTR; cb-unc-119(+)]IV #1*	This study	DKC1057
dhaSI145 [oxTi185; pDC973; Pdes-2--TIR1--F2A--mTagBFP--AID--NLS--tbb-23'UTR; cb-unc-119(+)]I #1; dhaSi89 [pDC747; Punc-86::TIR-1::unc543'UTR; cb-unc-119(+)]II #1; dhaSi243[pDC929; oxTi365; Pdes-2--LifeAct-mKate2--tbb-2 3UTR; cb-unc-119(+)]IV #1; dhaSi45[oxTi365; pDC675; Pdes-2::mNG-PH::unc-54 3'UTR; cb-unc-119(+)] V clone A*	This study	DKC1087
dhaSI145 [oxTi185; pDC973; Pdes-2--TIR1--F2A--mTagBFP--AID--NLS--tbb-23'UTR; cb-unc-119(+)]I #1; dhaSi89 [pDC747; Punc-86::TIR-1::unc543'UTR; cb-unc-119(+)]II #1; knl-1(dha122 (AID::dTagmB>F>P::::KNL-1))III ; unc-119(ed3)III?; dhaSi243[pDC929; oxTi365; Pdes-2--LifeAct-mKate2--tbb-2 3UTR; cb-unc-119(+)]IV #15; pDC675; Pdes-2::mNG-PH::unc-54 3'UTR; cb-unc-119(+)] V clone A*	This study	DKC1113
dhaSI145 [oxTi185; pDC973; Pdes-2--TIR1--F2A--mTagBFP--AID--NLS--tbb-23'UTR; cb-unc-119(+)]I #1;tiam-1(ok772) I; dhaSi89 [pDC747; Punc-86::TIR-1::unc543'UTR; cb-unc-119(+)]II #1; knl-1(dha122 (AID::dTagmB>F>P::::KNL-1))III ; unc-119(ed3)III?; dhaSi243[pDC929; oxTi365; Pdes-2--LifeAct-mKate2--tbb-2 3UTR; cb-unc-119(+)]IV #1*	This study	DKC1103
tiam-1(ok772) I; dhaSi89 [pDC747; Punc-86::TIR-1::unc543'UTR; cb-unc-119(+)]II #1; unc-119(ed3)III?; dhaSi243[pDC929; oxTi365; Pdes-2--LifeAct-mKate2--tbb-2 3UTR; cb-unc-119(+)]IV #1	This study	DKC1109

dma-1 (dha155; DEL)I; dhaSi89 [pDC747; Punc-86::TIR-1::unc543'UTR; cb-unc-119(+)]II #1; dhaSi243[pDC929; oxTi365; Pdes-2--LifeAct-mKate2--tbb-2 3UTR; cb-unc-119(+)]IV #1	This study	DKC1145
dma-1 (dha155; DEL)I; dhaSi89 [pDC747; Punc-86::TIR-1::unc543'UTR; cb-unc-119(+)]II #1; knl-1(dha122 (AID::dTagmB>F>P::::KNL-1))III; dhaSi243[pDC929; oxTi365; Pdes-2--LifeAct-mKate2--tbb-2 3UTR; cb-unc-119(+)]IV #1	This study	DKC1147
dhaSI145 [oxTi185; pDC973; Pdes-2--TIR1--F2A--mTagBFP--AID--NLS--tbb-23'UTR; cb-unc-119(+)]I #1; dha149(HA::GFP11::tba-1)I; dhaSi89 [pDC747; Punc-86::TIR-1::unc543'UTR; cb-unc-119(+)]II #1; ; unc-119(ed3)III?; dhaSi76[oxTi177;PDC731; Pdes-2::mSca-PH::unc-54 3'UTR; cb-unc-119(+)] IV; dhaSi207 [pDC1020;unc-86pro::splitGFP1-10::tbb-2 3'UTR; cb-unc-119(+)] V #2*	This study	DKC1086
dhaSI145 [oxTi185; pDC973; Pdes-2--TIR1--F2A--mTagBFP--AID--NLS--tbb-23'UTR; cb-unc-119(+)]I #1; dha149(HA::GFP11::tba-1)I; dhaSi89 [pDC747; Punc-86::TIR-1::unc543'UTR; cb-unc-119(+)]II #1; knl-1(dha122 (AID::dTagmB>F>P::::KNL-1))III; unc-119(ed3)III?; dhaSi76[oxTi177;PDC731; Pdes-2::mSca-PH::unc-54 3'UTR; cb-unc-119(+)] IV; dhaSi207 [pDC1020;unc-86pro::splitGFP1-10::tbb-2 3'UTR; cb-unc-119(+)] V #2*	This study	DKC1090
dhaSI145 [oxTi185; pDC973; Pdes-2--TIR1--F2A--mTagBFP--AID--NLS--tbb-23'UTR; cb-unc-119(+)]I #1; dhaSi89 [pDC747; Punc-86::TIR-1::unc543'UTR; cb-unc-119(+)]II #1; knl-1(dha122 (AID::dTagmB>F>P::::KNL-1))III ; unc-119(ed3)III?; dhaSi76[oxTi177;PDC731; Pdes-2::mSca-PH::unc-54 3'UTR; cb-unc-119(+)] IV; dhaSi269[oxTi177; pDC1106 ;Pser-2prom3::ebp-2::gfp::tbb-2 3'UTR ; cb-unc-119(+)]V #1*	This study	DKC1072
dhaSI145 [oxTi185; pDC973; Pdes-2--TIR1--F2A--mTagBFP--AID--NLS--tbb-23'UTR; cb-unc-119(+)]I #1; dhaSi89 [pDC747; Punc-86::TIR-1::unc543'UTR; cb-unc-119(+)]II #1; unc-119(ed3)III?; dhaSi76[oxTi177;PDC731; Pdes-2::mSca-PH::unc-54 3'UTR; cb-unc-119(+)] IV; dhaSi269[oxTi177; pDC1106 ;Pser-2prom3::ebp-2::gfp::tbb-2 3'UTR ; cb-unc-119(+)]V #1*	This study	DKC1073
dhaSI145 [oxTi185; pDC973; Pdes-2--TIR1--F2A--mTagBFP--AID--NLS--tbb-23'UTR; cb-unc-119(+)]I #1; dhaSi89 [pDC747; Punc-86::TIR-1::unc543'UTR; cb-unc-119(+)]II #1; unc-119(ed3)III?; dhaSi76[oxTi177;PDC731; dhaSi237[oxTi177; pDC1061;Pser-2prom3::mscarlet::linker::LGG1:unc 54 3'UTR; cb-unc-119(+)]V #1*	This study	DKC1127
dhaSI145 [oxTi185; pDC973; Pdes-2--TIR1--F2A--mTagBFP--AID--NLS--tbb-23'UTR; cb-unc-119(+)]I #1; dhaSi89 [pDC747; Punc-86::TIR-1::unc543'UTR; cb-unc-119(+)]II #1; knl-1(dha122 (AID::dTagmB>F>P::::KNL-1))III ; unc-119(ed3)III?; dhaSi76[oxTi177;PDC731;dhaSi237[oxTi177; pDC1061;Pser-2prom3::mscarlet::linker::LGG1:unc 54 3'UTR; cb-unc-119(+)]V #1*	This study	DKC1126
dhaSI145 [oxTi185; pDC973; Pdes-2--TIR1--F2A--mTagBFP--AID--NLS--tbb-23'UTR; cb-unc-119(+)]I #1; dhaSi89 [pDC747; Punc-86::TIR-1::unc543'UTR; cb-unc-119(+)]II #1; unc-119(ed3)III?; unc-119 (ed3)III; dhaSi53[oxTi177;pDC675; Pdes-2::Mng-PH::unc-54 3'UTR; cb-unc-119 (+)]IV clone B; dhaSi237[oxTi177; pDC1061;Pser-2prom3::mscarlet::linker::LGG1:unc 54 3'UTR; cb-unc-119(+)]V #1*	This study	DKC1132
dhaSI145 [oxTi185; pDC973; Pdes-2--TIR1--F2A--mTagBFP--AID--NLS--tbb-23'UTR; cb-unc-119(+)]I #1; dhaSi89 [pDC747; Punc-86::TIR-1::unc543'UTR; cb-unc-119(+)]II #1; knl-1(dha122 (AID::dTagmB>F>P::::KNL-1))III ; unc-119(ed3)III?; unc-119 (ed3)III; dhaSi53[oxTi177;pDC675; Pdes-2::Mng-PH::unc-54 3'UTR; cb-unc-119 (+)]IV clone B; dhaSi237[oxTi177; pDC1061;Pser-2prom3::mscarlet::linker::LGG1:unc 54 3'UTR; cb-unc-119(+)]V #1*	This study	DKC1131
dma-1 (dha155; DEL)I	This study	DKC919

Table S2. CRISPR-Cas9 Protocol & sgRNA Sequences Used for Strain Generation

GENOTYPE	METHOD & REFERENCE	sgRNA SEQUENCE
knl-1(dha122 (AID::dTagmB>F>P::::KNL-1))III &knl-1(dha130; HA::7XGFP11::knl-1)III	Ribonucleoprotein complex (Paix, et al., 2015)	catatttacagccATGTCGA & CTTACGAGGCTCCATCGACA
dhaSi76[ndc-80(dha148; NDC-80::AID::dgfp^3XFLAG)	SEC (Dickinson et al., 2015)	ATGTGCTGGCATTGAAAAGG
dma-1 (dha155; DEL)I	Ribonucleoprotein complex (Paix, et al., 2015)	agctagaagcagcaaacgtg & GGTGCTGGTGGAATCAATGG

REFERENCES

608 1. Jan, Y.N., and Jan, L.Y. (2001). Dendrites. Genes Dev. *15*, 2627–2641.

609 2. Jan, Y.N., and Jan, L.Y. (2010). Branching out: mechanisms of dendritic arborization.
610 Nat. Rev. Neurosci. *11*, 316–328.

611 3. Li, Z., Van Aelst, L., and Cline, H.T. (2000). Rho GTPases regulate distinct aspects of
612 dendritic arbor growth in Xenopus central neurons in vivo. Nat. Neurosci. *3*, 217–225.

613 4. Luo, L., Hensch, T.K., Ackerman, L., Barbel, S., Jan, L.Y., and Jan, Y.N. (1996).
614 Differential effects of the Rac GTPase on Purkinje cell axons and dendritic trunks and
615 spines. Nature *379*, 837–840.

616 5. Threadgill, R., Bobb, K., and Ghosh, A. (1997). Regulation of dendritic growth and
617 remodeling by Rho, Rac, and Cdc42. Neuron *19*, 625–634.

618 6. Nakayama, A.Y., Harms, M.B., and Luo, L. (2000). Small GTPases Rac and Rho in the
619 maintenance of dendritic spines and branches in hippocampal pyramidal neurons. J.
620 Neurosci. *20*, 5329–5338.

621 7. Scott, E.K., and Luo, L. (2001). How do dendrites take their shape? Nat. Neurosci. *4*,
622 359–365.

623 8. Lefebvre, J.L. (2021). Molecular mechanisms that mediate dendrite morphogenesis.
624 Curr. Top. Dev. Biol. *142*, 233–282.

625 9. Sundararajan, L., Stern, J., and Miller, D.M., 3rd (2019). Mechanisms that regulate
626 morphogenesis of a highly branched neuron in C. elegans. Dev. Biol. *451*, 53–67.

627 10. Taylor, C.A., Yan, J., Howell, A.S., Dong, X., and Shen, K. (2015). RAB-10 Regulates
628 Dendritic Branching by Balancing Dendritic Transport. PLoS Genet. *11*, e1005695.

629 11. Maniar, T.A., Kaplan, M., Wang, G.J., Shen, K., Wei, L., Shaw, J.E., Koushika, S.P., and
630 Bargmann, C.I. (2012). UNC-33 (CRMP) and ankyrin organize microtubules and localize
631 kinesin to polarize axon-dendrite sorting. Nat. Neurosci. *15*, 48–56.

632 12. Jaworski, J., Kapitein, L.C., Gouveia, S.M., Dortland, B.R., Wulf, P.S., Grigoriev, I.,
633 Camera, P., Spangler, S.A., Di Stefano, P., Demmers, J., et al. (2009). Dynamic
634 microtubules regulate dendritic spine morphology and synaptic plasticity. Neuron *61*, 85–
635 100.

636 13. Cao, Y., Lipka, J., Stucchi, R., Burute, M., Pan, X., Portegies, S., Tas, R., Willems, J.,
637 Will, L., MacGillavry, H., et al. (2020). Microtubule Minus-End Binding Protein CAMSAP2
638 and Kinesin-14 Motor KIFC3 Control Dendritic Microtubule Organization. Curr. Biol. *30*,
639 899-908.e6.

640 14. Kahn, O.I., Schätzle, P., van de Willige, D., Tas, R.P., Lindhout, F.W., Portegies, S.,
641 Kapitein, L.C., and Hoogenraad, C.C. (2018). APC2 controls dendrite development by
642 promoting microtubule dynamics. Nat. Commun. *9*, 2773.

643 15. Nguyen, M.M., McCracken, C.J., Milner, E.S., Goetschius, D.J., Weiner, A.T., Long,
644 M.K., Michael, N.L., Munro, S., and Rolls, M.M. (2014). Γ-tubulin controls neuronal
645 microtubule polarity independently of Golgi outposts. Mol. Biol. Cell *25*, 2039–2050.

646 16. Merriam, E.B., Lumbard, D.C., Viesselmann, C., Ballweg, J., Stevenson, M., Pietila, L.,
647 Hu, X., and Dent, E.W. (2011). Dynamic microtubules promote synaptic NMDA receptor-
648 dependent spine enlargement. PLoS One *6*, e27688.

649 17. Hu, X., Viesselmann, C., Nam, S., Merriam, E., and Dent, E.W. (2008). Activity-
650 dependent dynamic microtubule invasion of dendritic spines. J. Neurosci. *28*, 13094–
651 13105.

652 18. Cheerambathur, D.K., and Desai, A. (2014). Linked in: formation and regulation of
653 microtubule attachments during chromosome segregation. Curr. Opin. Cell Biol. *26*, 113–
654 122.

655 19. Musacchio, A., and Desai, A. (2017). A Molecular View of Kinetochore Assembly and
656 Function. Biology *6*, 5.

657 20. Cheerambathur, D.K., Prevo, B., Chow, T.-L., Hattersley, N., Wang, S., Zhao, Z., Kim,
658 T., Gerson-Gurwitz, A., Oegema, K., Green, R., et al. (2019). The Kinetochore-
659 Microtubule Coupling Machinery Is Repurposed in Sensory Nervous System
660 Morphogenesis. Dev. Cell *48*, 864-872.e7.

661 21. Zhao, G., Oztan, A., Ye, Y., and Schwarz, T.L. (2019). Kinetochore Proteins Have a Post-
662 Mitotic Function in Neurodevelopment. Dev. Cell *48*, 873-882.e4.

663 22. Hertzler, J.I., Simonovitch, S.I., Albertson, R.M., Weiner, A.T., Nye, D.M.R., and Rolls,
664 M.M. (2020). Kinetochore proteins suppress neuronal microtubule dynamics and
665 promote dendrite regeneration. Mol. Biol. Cell *31*, 2125–2138.

666 23. Smith, C.J., Watson, J., Spencer, W.C., O'Brien, T., Cha, B., Albeg, A., Treinin, M., and
667 Miller, D.M., III (2010). Time-lapse imaging and cell-specific expression profiling reveal
668 dynamic branching and molecular determinants of a multi-dendritic nociceptor in C.
669 elegans. Dev. Biol. *345*, 18–33.

670 24. Kamiyama, D., Sekine, S., Barsi-Rhyne, B., Hu, J., Chen, B., Gilbert, L.A., Ishikawa, H.,
671 Leonetti, M.D., Marshall, W.F., Weissman, J.S., et al. (2016). Versatile protein tagging in
672 cells with split fluorescent protein. Nat. Commun. *7*, 929.

673 25. Nishimura, K., Fukagawa, T., Takisawa, H., Kakimoto, T., and Kanemaki, M. (2009). An
674 auxin-based degron system for the rapid depletion of proteins in nonplant cells. Nat.
675 Methods *6*, 917–922.

676 26. Ashley, G.E., Duong, T., Levenson, M.T., Martinez, M.A.Q., Johnson, L.C., Hibshman,
677 J.D., Saeger, H.N., Palmisano, N.J., Doonan, R., Martinez-Mendez, R., et al. (2021). An
678 expanded auxin-inducible degron toolkit for Caenorhabditis elegans. Genetics *217*.
679 10.1093/genetics/iyab006.

680 27. Liao, C.-P., Li, H., Lee, H.-H., Chien, C.-T., and Pan, C.-L. (2018). Cell-Autonomous
681 Regulation of Dendrite Self-Avoidance by the Wnt Secretory Factor MIG-14/Wntless.
682 Neuron *98*, 320-334.e6.

683 28. E, L., Zhou, T., Koh, S., Chuang, M., Sharma, R., Pujol, N., Chisholm, A.D., Eroglu, C.,
684 Matsunami, H., and Yan, D. (2018). An Antimicrobial Peptide and Its Neuronal Receptor
685 Regulate Dendrite Degeneration in Aging and Infection. Neuron *97*, 125-138.e5.

686 29. He, L., Kooistra, R., Das, R., Oudejans, E., van Leen, E., Ziegler, J., Portegies, S., de
687 Haan, B., van Regteren Altena, A., Stucchi, R., et al. (2020). Cortical anchoring of the
688 microtubule cytoskeleton is essential for neuron polarity. Elife *9*. 10.7554/eLife.55111.

689 30. He, L., van Beem, L., Snel, B., Hoogenraad, C.C., and Harterink, M. (2022). PTRN-1
690 (CAMSAP) and NOCA-2 (NINEIN) are required for microtubule polarity in Caenorhabditis
691 elegans dendrites. PLoS Biol. *20*, e3001855.

692 31. Harterink, M., Edwards, S.L., de Haan, B., Yau, K.W., van den Heuvel, S., Kapitein, L.C.,
693 Miller, K.G., and Hoogenraad, C.C. (2018). Local microtubule organization promotes
694 cargo transport in C. elegans dendrites. J. Cell Sci. *131*, jcs223107.

695 32. Zou, W., Dong, X., Broederdorf, T.R., Shen, A., Kramer, D.A., Shi, R., Liang, X., Miller,
696 D.M., III, Xiang, Y.K., Yasuda, R., et al. (2018). A Dendritic Guidance Receptor Complex
697 Brings Together Distinct Actin Regulators to Drive Efficient F-Actin Assembly and
698 Branching. Dev. Cell *45*, 362-375.e3.

699 33. Tang, L.T., Diaz-Balzac, C.A., Rahman, M., Ramirez-Suarez, N.J., Salzberg, Y., Lázaro-
700 Peña, M.I., and Bülow, H.E. (2019). TIAM-1/GEF can shape somatosensory dendrites
701 independently of its GEF activity by regulating F-actin localization. Elife *8*.
702 10.7554/eLife.38949.

703 34. Yan, J., Chao, D.L., Toba, S., Koyasako, K., Yasunaga, T., Hirotsune, S., and Shen, K.
704 (2013). Kinesin-1 regulates dendrite microtubule polarity in Caenorhabditis elegans. Elife
705 *2*, 153.

706 35. Sundararajan, L., Smith, C.J., Watson, J.D., Millis, B.A., Tyska, M.J., and Miller, D.M.,
707 3rd (2019). Actin assembly and non-muscle myosin activity drive dendrite retraction in
708 an UNC-6/Netrin dependent self-avoidance response. PLoS Genet. *15*, e1008228.

709 36. Cheng, L., Zhang, J., Ahmad, S., Rozier, L., Yu, H., Deng, H., and Mao, Y. (2011). Aurora
710 B regulates formin mDia3 in achieving metaphase chromosome alignment. Dev. Cell *20*,
711 342–352.

712 37. Mogessie, B., and Schuh, M. (2017). Actin protects mammalian eggs against
713 chromosome segregation errors. Science *357*. 10.1126/science.aal1647.

714 38. Yasuda, S., Oceguera-Yanez, F., Kato, T., Okamoto, M., Yonemura, S., Terada, Y.,
715 Ishizaki, T., and Narumiya, S. (2004). Cdc42 and mDia3 regulate microtubule attachment
716 to kinetochores. Nature *428*, 767–771.

717 39. Harasimov, K., Uraji, J., Mönnich, E.U., Holubcová, Z., Elder, K., Blayney, M., and Schuh,
718 M. (2023). Actin-driven chromosome clustering facilitates fast and complete
719 chromosome capture in mammalian oocytes. Nat. Cell Biol. 10.1038/s41556-022-01082-
720 9.

721 40. Frøkjaer-Jensen, C., Davis, M.W., Hopkins, C.E., Newman, B.J., Thummel, J.M.,
722 Olesen, S.-P., Grunnet, M., and Jorgensen, E.M. (2008). Single-copy insertion of
723 transgenes in Caenorhabditis elegans. Nat. Genet. *40*, 1375–1383.

724 41. Dickinson, D.J., Ward, J.D., Reiner, D.J., and Goldstein, B. (2013). Engineering the
725 Caenorhabditis elegans genome using Cas9-triggered homologous recombination. Nat.
726 Methods *10*, 1028–1034.

727 42. Waaijers, S., Portegijs, V., Kerver, J., Lemmens, B.B.L.G., Tijsterman, M., van den
728 Heuvel, S., and Boxem, M. (2013). CRISPR/Cas9-Targeted Mutagenesis in
729 Caenorhabditis elegans. Genetics *195*, 1187–1191.

730 43. Paix, A., Folkmann, A., Rasoloson, D., and Seydoux, G. (2015). High Efficiency,
731 Homology-Directed Genome Editing in Caenorhabditis elegansUsing CRISPR-Cas9
732 Ribonucleoprotein Complexes. Genetics *201*, 47–54.

733 44. Gibson, D.G., Young, L., Chuang, R.-Y., Venter, J.C., Hutchison, C.A., and Smith, H.O.
734 (2009). Enzymatic assembly of DNA molecules up to several hundred kilobases. Nat.
735 Methods *6*, 343–345.

736 45. Mangeol, P., Prevo, B., and Peterman, E.J.G. (2016). KymographClear and
737 KymographDirect: two tools for the automated quantitative analysis of molecular and
738 cellular dynamics using kymographs. Mol. Biol. Cell *27*, 1948–1957.